EAST EUROPEAN JOURNAL OF PHYSICS. 4. 469-490 (2024)
DOI:10.26565/2312-4334-2024-4-57 ISSN 2312-4334

ENHANCEMENT OF MOLECULAR STRUCTURAL AND LINEAR/NONLINEAR OPTICAL FEATURES OF CHITOSAN/TITANIUM DIOXIDE NANOCOMPOSITE FILMS FOR FOOD PACKAGING AND OPTOELECTRONIC APPLICATIONS

Osiris W. Guirguis[a]*, Najlaa D. Alharbi[b]
[a]*Biophysics Department, Faculty of Science, Cairo University, Giza, Egypt*
[b]*Department of Physical Sciences, College of Science, University of Jeddah, Jeddah, Saudi Arabia*
**Corresponding Author e-mail: osiris@sci.cu.edu.eg*
Received July 2, 2024; revised September 18, 2024; accepted October 9, 2024

The current study aims to synthesize and characterize nanocomposite films of chitosan and titanium dioxide in terms of molecular structure, thermal and optical properties for use in food packaging and optoelectronic applications. The Fourier-transform infrared (FTIR) spectroscopy was used to study the interaction between the TiO_2-NPs and chitosan and the analysis confirmed that TiO_2-NPs interacted with chitosan and demonstrated good compatibility. Differential scanning calorimetry and thermogravimetric analysis revealed that increasing the concentration of TiO_2-NPs improved the thermal stability of the nanocomposites. The linear optical properties in the UV-Vis range (200–800 nm) were measured spectrophotometrically. Below 400 nm, the transmittance spectra of the nanocomposites show decreased degrees of transparency, indicating their capacity to entirely block UV-light transmission. Tauc's model was used to identify the types of electronic transitions in the samples. The single-oscillator model was utilized to investigate the dispersion energy and parameters. Nonlinear optical properties were also investigated. UV-Vis in the region (360-410 nm), the analysis revealed that increasing the concentration of TiO_2-NPs from 0 to 12 wt% reduced the absorption edge from 2.716 to 2.043 eV, decreased the direct (3.282 to 2.798 eV) and indirect (2.417 to 1.581 eV) energy band gaps, increased the Urbach energy from 0.692 to 1.295 eV, decreased the dispersion energy from 11.324 to 5.621 eV, decreased the single oscillator energy from 6.308 to 5.393 eV, and improved the other linear and nonlinear parameters. The findings support the usage of CS/TiO_2 nanocomposite films in the packaging industry and a variety of optical applications.
Keywords: *Chitosan; TiO_2 Nanoparticles; Chitosan/TiO_2 Nanocomposites; FTIR Analysis; Thermal Stability; Linear/nonlinear Optical Properties*
PACS: 78.20.Ci; 36.20.Kd; 73.50.Gr; 77.22._d; 78.30.Jw

1. INTRODUCTION

Polymers and nanocomposites have grown in importance due to their wide range of applications, including photonics, biotechnology, packaging, drug delivery, and optoelectronics [1,2]. Overuse of synthetic polymers and nanocomposites in the packaging sector has become a severe global environmental problem in recent decades due to their nonbiodegradability [3,4]. The increasing concern about the environment has prompted the industry to try to replace non-biodegradable petrochemical-based plastics with biodegradable ones. Strategies for improving biopolymer characteristics involve matrix reinforcement. Some package optimization solutions have been proposed, including altering pack sizes and constructing active and intelligent packaging that preserves food quality while increasing shelf life [5,6]. Polymer/biopolymer composites, on the other hand, have been shown to function as passive or active optical components in optoelectronics [7,8]. Furthermore, nanocomposites are useful and have been used in a variety of sectors, including physical, biological, biomedical, and pharmacological applications. They can be utilized in films having a high index of refraction, thin film transistors, solar cells, light-emitting diodes, optical waveguides, and photochromic materials. Biopolymers derived from biomass, including proteins, polysaccharides, and biodegradable polymers, are commonly employed in the fabrication of bio-based films and thin membranes [9-11]. The combination of diverse polymers, organic and/or inorganic particles, and polymers is a strategic approach to improving material performance and enabling the creation of unique composite systems that increase the performance of the parent polymer. One way for creating a novel material with diverse properties is to mix solutions of several polymers together. These qualities are primarily determined by the properties of the original homopolymers as well as the compound makeup. Recently, there has been a hunt for newer materials for sophisticated technology that have fixed properties. Organic and polymeric materials have been the subject of much research as promising candidate media for optical information transmission, optical data storage, optical switching, and processing [12]. The organic compound has special applications, particularly in nonlinear optics (NLO), electronic/optoelectronic materials, and optical communication. All nonlinear optics research works to develop a material with good nonlinear optical (NLO) properties while also meeting all technological requirements [12,13]. NLO materials, which have a large nonlinear absorption coefficient that is primarily determined by the imaginary part of the third-order nonlinear susceptibility and a higher nonlinear refractive index that is directly related to the real part of the third-order nonlinear susceptibility, are used in optical limiting and optical switching technology [14].

Cite as: O.W. Guirguis, N.D. Alharbi, East Eur. J. Phys. 4, 469 (2024), https://doi.org/10.26565/2312-4334-2024-4-57

Polysaccharides utilized to make edible films include cellulose, starch derivatives, pectin derivatives, seaweed extracts, microbial fermentation gums, and chitosan [15]. The future potential of biopolymers, particularly those derived from renewable resources, has long been recognized. These biopolymers are predominantly employed in the food industry. Biopolymers used as coatings in food packaging offer the benefits of being biocompatible, biodegradable, and increasing the quality of fresh foods while also being environmentally friendly packaging. Chitosan, a deacetylated derivative of chitin, is a well-known biopolymer and the second most abundant linear polysaccharide after cellulose [16-19]. Chitosan is a renewable substance derived from crustacean skeletons (crab, shrimp, and lobster), molluscan organs, the exoskeleton of marine zooplankton species such as coral and jellyfish, insect cuticles (butterflies and ladybugs), yeast cell walls, some mushroom envelopes, and fungi [20,21]. Chitosan's main-chain contains highly reactive hydroxyl (–OH) and high-density amine ($–NH_2$) groups, which can donate a free pair of electrons, make it soluble in diluted aqueous acetic solvents, and make it useful in a variety of applications and readily available for chemical reactions. Chitosan biopolymer is an attractive substance that is thought to be a great adsorbent due to its high nitrogen and oxygen content [22]. Chitosan can be made in a variety of geometries, including films, microspheres, nanospheres, and sponges. Chitosan's chemical and biological properties include being biocompatible with living tissues, biodegradable, bioadhesive, absorbable, nontoxic, a good film-forming biopolymer, naturally decomposed by body enzymes, and capable of binding to metal ions [23-26]. Chitosan's unique qualities make it useful in a wide range of biotechnological applications, including medical and environmental protection. It has been discovered in industrial and agricultural fields, either alone or in combination with other natural polymers [27-31]. Chitosan's polycationic structure makes it effective for immunoadjuvant, anti-thrombogenic, immunoenhancing, antitumoral, antiviral, antibacterial, antifungal, non-allergic, and anti-cholesteric properties [26,31,32]. Chitosan has been thoroughly researched for various potential uses including pharmaceutical, drug and gene delivery, dressings for wounds, treatment for cancer, burned skin, skin natural regeneration, functional coatings, beauty products, biological engineering, surgical tools, food industries, filtration of water for heavy metal adsorption, juice clarification and deacidification, food extended shelf life and preserving from microbial deterioration, food quality advancement, additives for food, and biodegradable packaging films formation [32-35]. Pieklarz and Modrzejewska [36] suggested that chitosan-based treatments could be used to prevent and treat viral infections, including COVID-19, due to their antiviral properties. The US-Food and Drug Administration (US-FDA) has designated chitosan as a generally recognized as safe (GRAS) food additive [28]. The hydrophilic characteristics of chitosan and other biopolymer films may limit their practical applications. Composite chitosan films exhibited superior hydrophobic properties compared to pure films [37]. Chitosan-based films, made through casting, can be utilized as active food packaging with added components and are considered safe food preservatives globally [28,32]. Combining chitosan with other biopolymers can increase its packaging material characteristics [38,39].

Nanoparticles (NPs) research has increased dramatically in recent years. Nanotechnology is concerned with the production and application of metal and metal oxide nanoparticles up to 100 nm in size. Because of their small size and unique features, metal and metal oxide nanoparticles have gained popularity in recent years. Nanoparticles have unique properties based on their size, shape, and morphology, allowing them to interact with plants, animals, and microbes [40-42]. Nanoparticles (NPs) are widely used in a variety of applications, including materials science, paints, agriculture, food industries, cosmetics, medicine delivery, and diagnostics [43,44]. They are also finding use in biomedicine, electronics, photography, optical electronics, optical data storage, information technology, biological sensing, and catalysis [21,43,45,46]. Inorganic metal NPs such as Fe, Cu, Ti, Ag, Au, Pt, and Zn, as well as metal oxide NPs such as CaO, CuO, ZnO, FeO, SiO_2, and TiO_2, have been shown to be potentially useful compounds due to their appealing characteristics [28,44,47,48]. The dispersion of nanoparticles in the polymer matrix is critical for increasing structural, optical, and mechanical properties. TiO_2 is a flexible and chemically inert metal oxide that has shown promise due to its photocatalytic activity, high chemical stability, cheap cost, biocompatibility, and antibacterial properties [5,49,50]. TiO_2 is commonly employed in a variety of applications, including medicinal, biomedical, antibacterial, ethylene scavenger, ecological, and clean energy [28,51]. In addition, the US-FDA has approved TiO_2 for use in human food, medicines, and products that contact food [52].When being subjected to UV-light at wavelengths <385 nm, TiO_2 produces reactive oxygen species like hydroxyl radicals (•OH), and superoxide ions (O_2^{*-}), capable of destroying microbial cells and killing microorganisms, as well as ethylene ultraviolet degradation [28]. According to Mohammad et al. [43], TiO_2-NPs and ZnO-NPs effectively scatter UV radiation and have been found to be particularly useful as UV blockers, which assist in protecting against skin cancer caused primarily by UV radiation, as well as photocatalysts in solar cells, exhibits and detectors, photosynthesis, and sunlight protection. Numerous research has reported that TiO_2nanoparticles at low content (≤5%) can enhance the physical-thermal properties of biocomposite films [28,31,53]. TiO_2-NPs have attracted consideration in the oil and gas industry because of their potential for purifying water and, more recently, as additives in recovery fluids to improve current improved oil recovery methods by modifying the surface tension or interfacial interactions [54-57]. One of the main downsides of TiO_2-NPs is their propensity to agglomerate, which reduces their photocatalytic ability [28]. According to Anaya Esparza et al. [51], the interaction of TiO_2-NPs with biopolymers such as starch, gums, and chitosan can aid to minimize TiO_2 spontaneous agglomeration, hence improving the functional aspects of composites.

On the other hand, the antibacterial, moisturizing, mechanical, and antioxidant capabilities of pure chitosan film have been deemed inadequate in practical applications. To overcome these limitations, metal oxide NPs were added

during film creation to create chitosan-based composite films with good physicochemical and biological properties [5,58,59]. Thus, composite films made of chitosan reinforced with nanoparticles have received a lot of attention for a variety of applications [11,15]. Recently, there has been a surge of interest in hybrid composites and their prospective applications, particularly CS/TiO_2 nanocomposites, which have intriguing technical characteristics as well as potential applications [5,24,51]. A number of research studies have reported that incorporating TiO_2-NPs into chitosan raised hydrophilicity, enhanced the mechanical characteristics of the composite film, reduced the transmission of light in the range of visible light, and indicated to be announcing composites in a variety of applications [5,28,51,60-63]. These CS/TiO_2 nanocomposites have applications in the biomedical field as scaffolding compounds for liver tissue engineering, clinical skincare as functional antimicrobial substances such as photobacteriocidal and artificial skin alternatives, restored tissues, healing of wounds, cancer detection and therapy, developed delivery of drugs, operating aids, and biological sensors for extracted fruits [31,43,51,64]. Razzaz et al. [65] and Spoială et al. [66] observed that CS functionalized with TiO_2 nanoparticles displayed adsorbent properties for treating wastewater for the elimination of heavy metal ions; Saravanan et al. [67] reported that CS/TiO_2 nanocomposites showed great effectiveness in degrading against methyl orange dye; Kaewklin et al. [17] achieved success in fabricating CS/TiO_2 nanocomposite films for tomato conservation; and Siripatrawan and Kaewklin [64] created and analyzed multifunctional active packaging for food using CS/TiO_2 nanocomposites for use as an antibacterial film in postharvest uses for preserving fresh produce.

In order to achieve the current study's objective, and in continuation of previous studies, especially by the same author(s), which were published previously, and with the addition of some theoretical analyses of the results obtained for the possibility of applying these compounds in many medical and industrial fields, the solution casting process was used for preparing pure CS and CS/TiO_2 nanocomposite films with various TiO_2-NP concentrations (4, 8, and 12 wt%). The molecular structure of the films was examined with the FTIR technique. DSC and TGA/DTGA thermograms were used to assess the thermal stability of the films. The kinetic parameters were evaluated using the Coat-Refdfern method. The optical characteristics of the produced nanocomposite films were measured spectroscopically in the UV-Vis range (200-800 nm). The linear optical parameters, including absorption coefficient (α), extinction coefficient (K), and refractive index (n), as well as dispersion parameters such as dispersion energy (E_d) and average energy gap (E_o), were determined. The films' nonlinear optical properties, including third-order susceptibility ($\chi^{(3)}$), refractive index (n_2), and absorption coefficient (β_c), were also evaluated. The results were discussed, and the potential for employing the produced nanocomposite films in biodegradable food packaging and optoelectronic applications was investigated.

2. EXPERIMENTAL PART

Materials and preparation of CS and CS/TiO_2 nanocomposite films

Chitosan (CS) powder with a molecular weight of 900 $kg.mol^{-1}$, particle size >100 mesh, deacetylation >75%, free of E. coli and Salmonella, creamy white color, odorlessness, and purity >98% was acquired from Avondale Laboratories Supplies & Services Ltd. Titanium dioxide (TiO_2) nanopowder with a particle size <100 nm (catalog number 718467), white color, and purity >99% was supplied from Sigma-Aldrich (China). Glacial acetic acid was obtained from Avondale Laboratories Supplies & Services Ltd. (Banbury, UK).

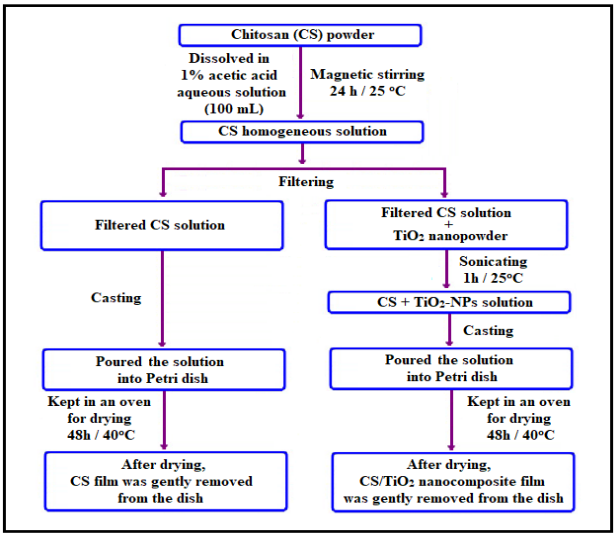

Figure 1. Flowchart of the process used to prepare CS and CS/TiO_2 nanocomposite films by casting technique

The film casting technique was used to manufacture pure chitosan (CS) and CS/TiO_2 nanocomposite films [5,8,50]. To prepare the chitosan (CS) film, dissolve 1 g of chitosan powder in 100 mL of a 1% (v/v) acetic acid aqueous solution. Stir continuously with a magnetic stirrer (100 rpm) for 24 hours at room temperature (~25°C). Filtration was used to remove the insoluble masses from the dissolved solution. CS thin films were produced by casting the solution onto Petri dishes and drying in an oven at 40°C for 48 hours before peeling off from the plate. For the preparation of the CS/TiO_2 nanocomposite films, various weights of TiO_2-NPs (0.04 g, 0.08 g, and 0.12 g) were added to the as-prepared CS solutions. The solutions were thoroughly mixed before being sonicated for 1 hour using a digital ultrasonic cleaner (CD-4820 170W/42 kHz, China) to eliminate agglomeration and achieve homogeneous solutions [5,8]. The solutions were then poured into Petri dishes and dried in an oven at 40°C for 48 hours. After drying, the films were gently removed from the plates and stored in vacuum desiccators at room temperature until used. The thicknesses of the films were measured using an Insize 3109-25A Digital External Micrometer (China) with an accuracy of ±2 μm, covering a range of 0-25 mm. Figure 1 depicts a schematic of the casting technique employed in the current study to produce pure chitosan (CS) and CS/TiO_2 nanocomposite films.

Characterization methods

FTIR absorption spectra of CS and CS/TiO_2 nanocomposite films were measured using a Fourier transform infrared spectrometer (Nicolet-380, UK). Spectra were acquired in the 4000-400 cm^{-1} range at room temperature using 32 scans, with a resolution of 4 cm^{-1} and an accuracy of ±1%.

The differential scanning calorimetry (DSC) of the manufactured films was carried out with a differential scanning calorimeter (Shimadzu DSC-50, Japan) with a measuring temperature range of 25 to 650°C. Thermogravimetric analysis (TGA/DTGA) of the films was performed using a thermogravimetric analyzer (Shimadzu TGA-50H, Japan) with a measuring temperature range of 25-750°C. The thermograms were recorded in an atmosphere of nitrogen with a flow rate of 30 $cm^3 \cdot min^{-1}$and a heating rate of 10°C·min^{-1}. The starting sample weight was around 6.5 mg. The temperature at the maximum decomposition rate (T_m) and weight loss (%) were estimated for each decomposition stage for the samples using TGA and DTGA thermograms. Each sample was packed snugly into an aluminum pan, with an empty pan acting as a reference. Prior to analysis, the equipment was calibrated with calcium oxalate as a standard reference.

The UV-Vis optical absorbance, transmittance, and reflectance spectra of the prepared films were recorded at room temperature using a UV-Vis-NIR double beam spectrophotometer (Shimadzu V-530, Japan) covering the range 200–2500 nm with standard illumination "C" and a 2 nm bandwidth with accuracy ±0.05%. The collected spectra were used to determine linear and nonlinear optical characteristics, as well as related parameters.

3. RESULTS AND DISCUSSION

Fourier transform infrared (FTIR) spectroscopy

To determine the potential interaction between the TiO_2-NPs and the CS chains, FTIR spectra have been recorded in the 4000-400 cm^{-1} region. A comparison of the FTIR absorption spectra of pure CS and CS/TiO_2 nanocomposite films is shown in Figure 2.

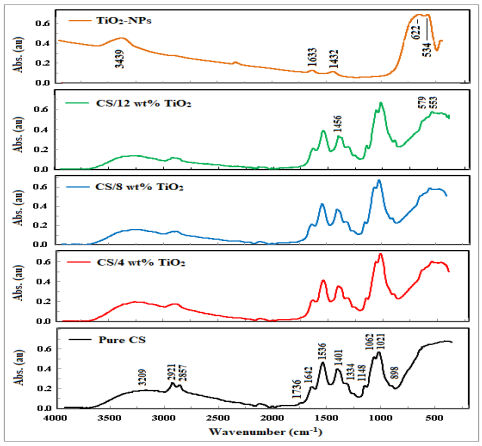

Figure 2. FTIR absorbance spectra of pure CS and CS/TiO_2 nanocomposite films

The FTIR spectra were in agreement with those previously reported by other researchers [32,37,39,45,51,55,64,66,68]. The broad absorption peak centered at around 3209 cm^{-1} was assigned to stretching vibrations of the hydroxyl (–OH) and amine (–NH) groups. The two peaks between 3000 and 2800 cm^{-1} (asymmetric at ~2921 cm^{-1} and symmetric at ~2857 cm^{-1}) were due to the C–H stretching vibration of the methyl group. The peak at ~1642 cm^{-1} was corresponded to C=O stretching vibration (amide I). The peak at ~1536 cm^{-1} was due to in plane N-H bending vibration (amide II). The peak at ~1401 cm^{-1} was assigned to deformation vibrations of C–H and –OH groups. The peaks in the range of 1150–1000 cm^{-1} were corresponded to asymmetric of C–O–C (at ~1148 cm^{-1}) and symmetric C-O (at ~1062 cm^{-1}) stretching vibrations. The peak at ~1021 cm^{-1} was assigned to C–O stretching vibration, and also indicated bending vibration of Ti–O–C. The weak peak at ~898 cm^{-1} was due to C–H stretching of the glycoside linkage and N–H (amide III). A shoulder corresponding to C–N stretching (amide III) at around 1334 cm^{-1} was observed. Furthermore, Hussein et al. [50] and Filippo et al. [69] identified two characteristic absorption peaks at approximately 1532 and 1456 cm^{-1}, corresponding to the symmetric and asymmetric stretching vibrations of the carboxyl groups, respectively. The figure also showed that all of the produced nanocomposite films had remarkably similar spectra, with mostly of the peak characteristic of the CS film. The FTIR spectra of pure CS and CS/TiO_2 nanocomposites show separate peaks for both CS and TiO_2-NPs in the composite. The spectra of the nanocomposites showed that the broader and stronger peak shifted somewhat to lower wavenumbers. The changes in spectra between the pure CS sample and the CS/TiO_2 nanocomposites revealed the interaction between CS and TiO_2-NPs due to minor differences in angles, bonding energies, internal stresses, and crystal level during the formation of the nanocomposites. As the concentration of TiO_2-NPs in the film increased, so did the small peaks at low wavenumbers in the range 700-500 cm^{-1} (at about 523-504 cm^{-1} and at ~680 cm^{-1}), indicating the bending vibration of Ti-O-Ti for the interactions of CS-TiO_2 [50,64,66]. A new shoulder was appeared at around 579 cm^{-1} belongs to the amide group and a new peak at ~553 cm^{-1} was formed corresponding to the

stretching group. This demonstrated that that –OH and/or $–NH_2$ from the CS chains can interact with the acidic groups of the TiO_2-NPs to establish covalent bonds or hydrogen bonds, hence improving TiO_2 nanoparticle incorporation in the CS matrix [5,28,70]. The findings suggest that TiO_2-NPs are primarily incorporated into the CS matrix in the amorphous area of chitosan [51,64].

The degree of structural organization of the films under study was evaluated using the following IR indices [71,72]: (1) the total crystallinity index (TCI), which provides the crystallinity ratio; (2) the lateral order index (LOI), which correlates the number of crystalline components and amorphous regions in the sample; and (3) the hydrogen bond intensity (HBI), which connects the crystalline structure and the degree of homogeneity of the molecules as measured by chain movement and bonding distance. TCI, LOI, and HBI can be assessed using the following relationships [73,74]:

$$\text{TCI} = \frac{H_{1336}}{H_{2896}}, \quad \text{LOI} = \frac{Ar_{1427}}{Ar_{896}}, \quad \text{and} \quad \text{HBI} = \frac{A_{3333}}{A_{1336}} \tag{1}$$

where H_{1336} and H_{2896} are the band heights of the O–H bending and C-H stretching vibrations, respectively, at 1336 and 2896 cm^{-1}; Ar_{1427} and Ar_{896} are the areas of the bands at 1427 and 896 cm^{-1}, respectively, which correspond to O–H, C-H bending, $–CH_2$deformation, C–O deformation, and $–CH_2$ rocking; A_{3333} and A_{1336} are the absorbance of the bands at 3333 and 1336 cm^{-1}, which correspond to the O–H stretching and bending vibration modes, respectively. Furthermore, the energy of the hydrogen bond (E_H) of the –OH stretch group was determined with the following formula [71,72,74]:

$$E_H = \left(\frac{1}{K}\right)\left(\frac{\upsilon_o - \upsilon}{\upsilon_o}\right) \tag{2}$$

where K is a constant (= 3.8095×10^{-6} J^{-1}), υ_o is the standard frequency of the free –OH group at 3650 cm^{-1}, and ν is the frequency of the bound –OH group of the sample. Table 1 shows the calculated values for the IR indices (TCI, LOI, and HBI), as well as E_H. It was discovered that the CS/12 wt% TiO_2 nanocomposite exhibited greater TCI and HBI values and a lower LOI value than other nanocomposites when compared to the pure CS sample, indicating decreased crystallinity. This observed tendency can be related to the differences in accessibility of the discrete crystalline and amorphous areas of the film, as well as its key chemical components. The table shows no discernible change (~5%) in E_H values between nanocomposites and pure CS samples. The presence of TiO_2-NPs on the CS network, as well as the formation of hydrogen bonds between CS and TiO_2-NPs, which increase the extent of hydrogen bonding between molecules in the CS, can be attributed to changes in the IR indices and E_H of the prepared nanocomposites [71,72].

Table 1. Values of TCL, LOI, HBI, and E_H for pure CS and CS/TiO_2 nanocomposites

Sample	TCL	LOI	HBI	E_H (kJ)
Pure CS	0.8293	48.3333	0.5751	31.6986
CS/4wt% TiO_2	1.1515	14.9608	0.5859	30.4212
CS/8wt% TiO_2	1.2074	12.2963	0.6226	30.3583
CS/12wt% TiO_2	1.4520	8.0494	0.7641	30.2668

Thermal properties

One of the most practical techniques for determining the miscibility and thermal properties of composite polymers was differential scanning calorimetry (DSC) [50]. Figure 3 depicts the DSC thermograms obtained to investigate the thermal behavior of pure CS and CS/TiO_2 nanocomposites. It was obvious that all films disintegrated in similar way up to 600°C.

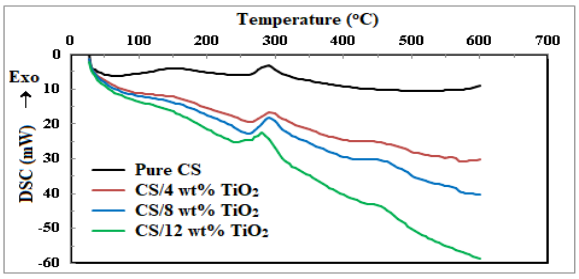

Figure 3. DSC thermograms of pure CS and CS/TiO_2 nanocomposite films

The thermogram for pure CS can be analyzed as follows: a broad endothermic peak between 25 and 125°C and an exothermic peak between 260 and 320°C [50,66]. The endothermic peak at ~65°C may be owing to the evaporation of water absorbed by the hydrophilic groups of chitosan [24]. The exothermic peak had a decomposition temperature of around 290°C, may be due to thermal decomposition of CS [24,66,75]. Furthermore, the thermograms of the

nanocomposite samples revealed one endothermic peak between 25 and 125°C and two exothermic peaks. The exothermic maxima ranged from 240 to 320°C and 420 to 480°C. The endothermic initial stage resulted in the loss of largely adsorbed water molecules. When TiO_2-NPs are dispersed in the CS matrix, the intensities of the exothermic peaks increase, which may correspond to weight loss caused by polysaccharide disintegration and loss of the hydroxyl group [50,76]. The area under the peak rose, indicating that the enthalpy of melting decreased as the amount of TiO_2-NPs increased. The decomposition temperature of the second stage shifts toward lower temperatures, showing the establishment of an intermolecular interaction and variation in internal mechanisms caused by the induced influence of TiO_2-NPs on the CS structure of the network.

Thermogravimetric analysis (TGA) is an extremely useful tool for determining the heat stability of polymers and nanocomposites [50,77,78]. Chitosan is highly sensitive to several types of degradation, including heat decomposition [11,24]. Figure 4 shows the TGA (a) and DTGA (b) thermograms of pure CS and CS/TiO_2 nanocomposite films at temperatures ranging from 25 to 750°C.

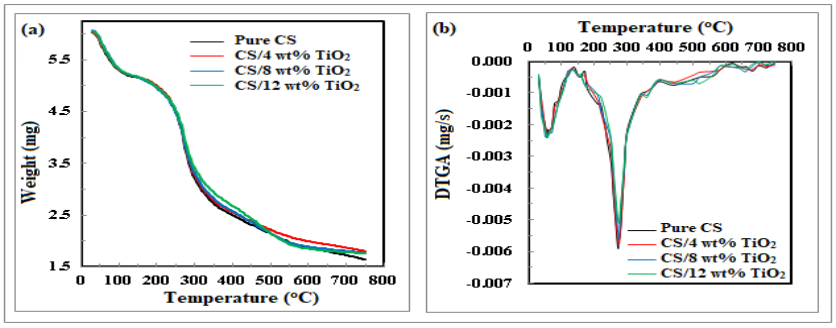

Figure 4. (a) TGA and (b) DTGA thermograms of pure CS and CS/TiO_2 nanocomposite films

DTGA curves represent the rate of weight loss during thermal degradation. Pure TiO_2-NPs in powder form remain stable up to 750°C (no curve depicted) [79]. As shown in Figure 4a, all films followed a similar decomposition approach, and the TGA thermograms reveal three stages of weight change [5,50,77,78]. A small weight loss was observed between 25 and 110°C, followed by a steady weight loss above 150 to 750°C. When the temperature reached 110°C, the weight loss during the first decomposition stage was approximately 13 to 10% of the original weight, which could be attributed to the vaporization of absorbed water and residual acetic acid in the polymer matrix [24,77,78,80]. Water absorption in the CS/TiO_2 nanocomposite was related to the presence of hydroxyl and amino groups, which interact with water molecules via hydrogen bonding. The second decomposition stage is more intense thermal deposition, which occurs at temperatures ranging from 150 to 400°C and results in a rapid weight loss of 44 to 42%, which could be attributed to the thermal and oxidative decomposition of the CS matrix (the main component of the nanocomposite) [66,80]. At temperatures above 400 to 750°C, films incorporating TiO_2-NPs experienced a third degradation step, resulting in a weight loss of around 16%. As previously described by Corazzari et al. [75], a crucial process connected with the pyrolytic disintegrate of chitosan was demonstrated in the temperature range of 200-450°C and entailed the release of H_2O, NH_3, CO, CO_2, and CH_3COOH. The second and third thermal stages may be caused by chain fragmentation, saccharide ring degradation, depolymerization, and the disintegration of acetylated and/or deacetylated chitosan units [8,80,81]. DTGA curves in Figure 4b show more accurate differences in the thermal behavior of CS and CS/TiO_2 nanocomposite films. Nearly no remarkable variation exists in the DTGA peak positions. The DTGA peak temperature of the pure CS sample was ~273°C [24], while the CS/TiO_2 nanocomposite had a peak temperature of ~274°C. Table 2 summarizes the maximum temperature (T_M), weight loss (%), total weight loss (%), and residual weight (%) values for CS and CS/TiO_2 nanocomposites at the three degradation stages. The residual weight of nanocomposites rose as the concentration of TiO_2-NPs increased, indicating that the presence of TiO_2-NPs changes the degradation mechanism of the CS matrix. Additionally, the nanocomposite films were more thermally stable than the CS sample. Many earlier studies have reported similar behavior [8,24,50,80]. In general, these findings validated the inclusion of TiO_2-NPs in the CS matrix of the produced films, which increases the thermal stability of the nanocomposite, and revealed that thermal stability was directly proportional to nanoparticle concentration.

Table 2. Maximum temperature (T_M), the weight loss (%) for the three decomposition stages, the total weight loss (%), and the residual weight (%) of pure CS and CS/TiO_2 nanocomposites

Sample	First stage (25-110 °C)		Second stage (110-400 °C)		Third stage (400-750 °C)	Total weight loss (%)	Residue (%)
	T_M (°C)	Weight loss (%)	T_M (°C)	Weight loss (%)	Weight loss (%)		
Pure CS	58.054	12.633	273.084	43.539	16.460	72.632	27.368
CS/4 wt% TiO_2	58.054	11.008	273.934	42.845	16.270	70.123	29.877
CS/8 wt% TiO_2	58.054	10.328	273.934	42.747	16.755	69.830	30.170
CS/12 wt% TiO_2	57.044	10.192	273.934	41.710	16.258	68.160	31.840

Kinetics of thermal decomposition

There is a growing interest in producing thermoplastic biopolymers, particularly those generated from renewable sources, for use in a variety of applications, including food packaging and optoelectronic devices. The TGA/DTGA technique plays an essential role for determining the decomposition processes, temperature, and kinetic characteristics of solid materials. The kinetics of thermal degradation processes were represented using different equations that took into account the unique properties of their mechanisms [8,82]. The activation energy for the primary thermal decomposition for TGA measurements can be calculated using the Coats and Redfern equation as follows [8,83]:

$$\ln\left(\frac{-\ln(1-g)^{1-n}}{T^2}\right) = -\frac{E_a}{RT} + \ln\left(\frac{fR}{qE_a}\right), \tag{3}$$

where T is the absolute temperature, g is the fractional weight loss at the specific temperature (T), n is the order of reaction, E_a is the activation energy, R is the universal gas constant (= 8.31445 $J.K^{-1}\cdot mol^{-1}$), q is the linear heating rate (dT/dt), and f is the frequency factor. The values of f and g can be estimated using the following formulae [8,82]:

$$g = \frac{w_i - w_T}{w_i - w_f}, \tag{4}$$

$$f = \frac{\gamma e k_B T_M}{h}\exp\left(\frac{\Delta S}{R}\right), \tag{5}$$

where w_i, w_T, and $w_f$are the initial mass, current mass at temperature T, and final mass of the sample, respectively, T_M is the maximum temperature of the decomposition stage, γ is the transmission coefficient (=1 for monomolecular reaction), e is the Neper number (=2.7183), h is the Planck's constant (=6.6261×10^{-34} J.s), k_B is the Boltzmann's constant (=1.3806×10^{-23} $J.K^{-1}$), and ΔS is the entropy activation. For $n \neq 1$, Eq. 3 can be rewritten as [8,82,83]:

$$\ln\left(\frac{-\ln(1-g)}{T^2}\right) = -\frac{E_a}{RT} + \ln\left(\frac{fR}{qE_a}\right). \tag{6}$$

Using Equation 5, ΔS can be estimated as follows [8]:

$$\Delta S = R\ln\left(\frac{fh}{\gamma e k_B T_M}\right). \tag{7}$$

The thermodynamic equations are used to compute the enthalpy activation (ΔH) for total thermal motion and the Gibbs free energy (ΔG) for system stability as follows [8]:

$$\Delta H = E_a - RT_M, \tag{8}$$

$$\Delta G = \Delta H - T_M\Delta S. \tag{9}$$

Figures 5 and 6 show the fluctuation of $\ln\left[-\ln(1-g)\right]/T^2$ against 1/T for pure CS and CS/TiO_2 nanocomposites throughout the first and second breakdown stages.

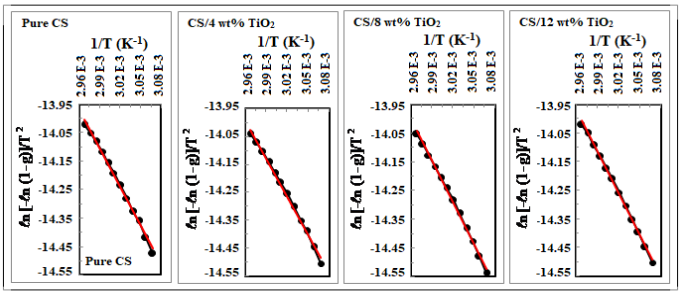

Figure 5. $\ln\left[-\ln(1-g)\right]/T^2$ against 1/T in the first decomposition stage for pure CS and CS/TiO_2 nanocomposite films

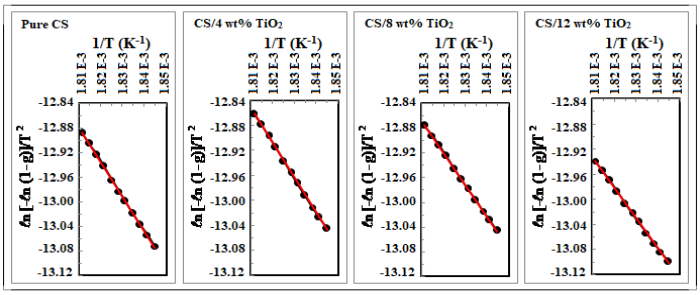

Figure 6. $\ln\left[-\ln(1-g)\right]/T^2$ against 1/T in the second decomposition stage for pure CS and CS/TiO_2 nanocomposite films

Table 3 summarizes the values of activation energy (E_a) and frequency factor (f) for all films based on the slope, intercept, and regression (r^2) of the fitted straight lines of each degradation stage. The values of ΔS, ΔH, and ΔG were computed using Equations. 7-9 and were listed in the table. The data in the table showed that the calculated activation energy values (E_a) of the nanocomposite samples increased in the first decomposition stage and decreased in the second as the TiO_2-NPs content increased, indicating that the nanocomposite sample had some form of chemical and/or physical rearrangement of the initial structure, bringing it into thermodynamic equilibrium.

Table 3. The kinetic parameters for of pure CS and CS/TiO_2 nanocomposites based on CR approach

Sample	E_a (kJ.mol^{-1})	f(Hz)	r^2	ΔS (kJ.mol^{-1}.K^{-1})	ΔH (kJ.mol^{-1})	ΔG (kJ.mol^{-1})
First decomposition stage						
CS	37.906	1.023×10^4	0.995	-0.177	35.145	94.049
CS/4wt% TiO_2	38.330	1.546×10^4	0.995	-0.174	35.577	93.151
CS/8wt% TiO_2	40.159	3.057×10^4	0.996	-0.168	37.406	93.1041
CS/12wt% TiO_2	40.334	3.379×10^4	0.998	-0.167	37.581	93.002
Second decomposition stage						
CS	46.669	1.748×10^3	0.999	-0.196	42.129	149.269
CS/4wt% TiO_2	46.503	1.724×10^3	0.999	-0.197	41.956	149.332
CS/8wt% TiO_2	43.1439	0.759×10^3	0.999	-0.203	38.596	149.706
CS/12wt% TiO_2	40.542	0.380×10^3	0.999	-0.209	35.994	150.251

According to the kinetic data from the DTGA curves (Figure 4b) and the data in Table 3, all of the nanocomposites exhibit negative activation entropy values, confirming that the generation of activated complexes is directly related to entropy variation. The association between E_a and f values in Table 3 verified the existence of the compensating phenomena, also known as the isokinetic effect [82] as illustrated in Figure 7a and b.

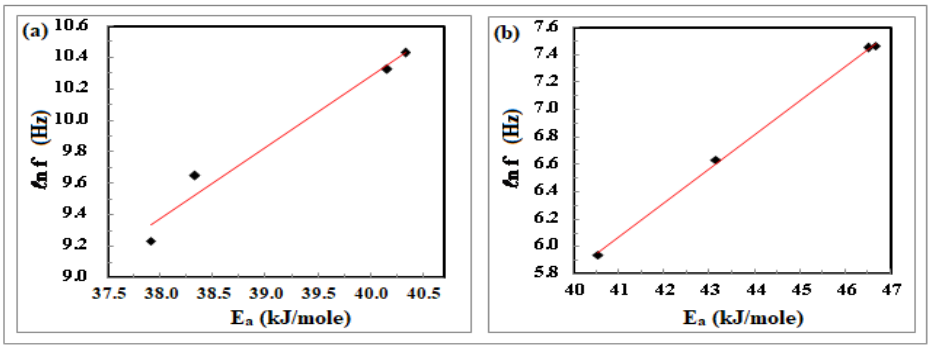

Figure 7. Frequency factor (f) versus the activation energy (E_a) in (a) first and (b) second decomposition stages for pure CS and CS/TiO_2 nanocomposite films

Figure 8a and b demonstrates a linear relationship between (ΔS) and (ΔH), indicating the presence of the compensating phenomena in CS/TiO_2 nanocomposites. This linear relation may be due to structural changes that occur when increasing the temperature of the polymeric material to achieve equilibrium. A similar tendency has already been seen for other polymer composites [8,84,85]. The acquired results could be employed in thermal degradation optimization, as well as to improve the thermal stability of the nanocomposite under examination, potentially leading to intriguing technological applications.

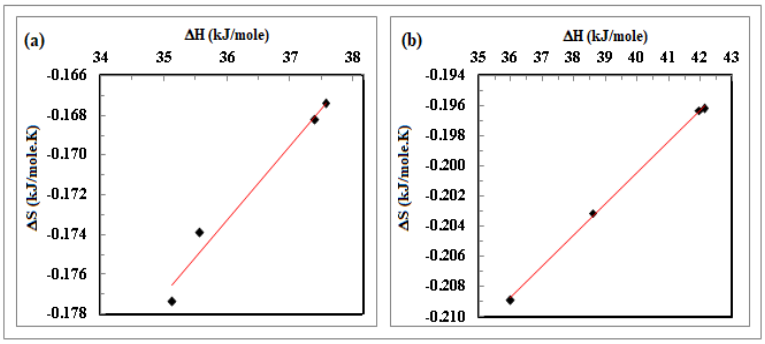

Figure 8. ΔS versus ΔH in (a) first and (b) second decomposition stages for pure CS and CS/TiO_2 nanocomposite films

UV-Vis optical characterization

The study of optical properties has significance for understanding the nature of materials utilized in food packaging and electrooptical applications. UV-Vis optical absorption spectra are one of the most effective tools for

revealing significant information about the films under investigation. Figure 9a depicts the absorption spectra of pure CS and CS/TiO_2 nanocomposites in the UV-Vis range of 200 to 800 nm.

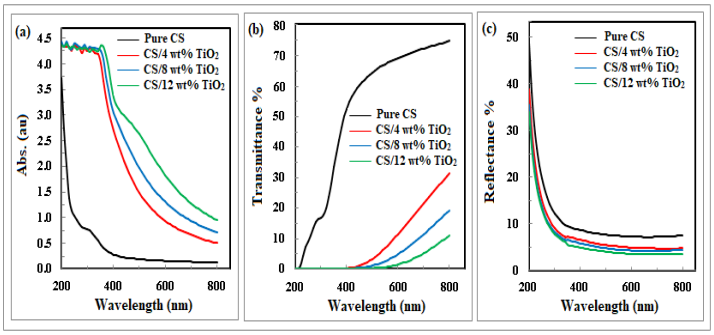

Figure 9. (a) Absorbance, (b) transmittance, and (c) reflectance spectra against wavelength for pure CS and CS/TiO_2 nanocomposite films

The absorption spectra for the films may be separated into two regions: 1) the first zone of significant absorption occurs between 200 and 360 nm, and 2) the second region of the absorption edge begins between 360 and 800 nm. The absorption spectra of pure CS decrease rapidly in the UV region as the wavelength increases, with an absorption shoulder centered at ~290 nm, corresponding to the forbidden n → π∗ transition. The absorbance decreases slightly in the visible range. As the amount of TiO_2-NPs in the nanocomposite film grows, the UV absorbance rises significantly, and the shoulder shifts to a longer wavelength. A new peak of TiO_2-NPs was identified at ~352 nm in the CS/12 wt% TiO_2 nanocomposite sample. This observation implies that the TiO_2-NPs and CS matrix are complexed via hydrogen bonding via OH groups [45]. In the visible region, absorbance increased as compared to pure CS film. This improvement is due in significant part to the addition of TiO_2-NPs at a concentration of 12 weight %. These observed increases in absorbance across the entire UV-Vis range (200-800 nm) can be attributed to an increase in composite film density, which leads to an increase in refractive index due to increased polarization. Figure 9b and c shows the spectrum characteristics of the optical transmittance and reflectance, respectively, of the produced films. Figure 9b indicates that the CS spectrum in the UV zone has transmittance values ranging from ~0.02 at 200 nm to ~38% at 360 nm. According to Souza et al. [3], chitosan film is an effective UV light barrier and they reported that T% values at 200 and 360 nm were approximately 0.02 and 38%, respectively. The spectra of the CS/TiO_2 nanocomposites show transmittance values close to 0% in the UV spectrum. The inclusion of TiO_2-NPs changed the barrier block at longer wavelengths. The optical transparency of the CS/12wt% TiO_2 nanocomposite decreased to ~0.005% at 360 nm, and UV light was nearly completely blocked. One of the most essential features of films designed for various food packaging categories is their UV-visible light barrier [3,86]. The acquired data reveal that all of the nanocomposite films under research have UV-blocking properties, making them suitable barriers against UV radiation and enhancing the shelf-life of light-sensitive foods by avoiding photo-oxidation [28,64]. Additionally, Figure 9a and b shows a considerable rise in absorption and decrease in transmittance across the whole spectrum as the concentration of TiO_2-NPs increased. This result could be attributable to a decrease in film transparency caused by variations in molecular composition [50]. Incorporating TiO_2-NPs with CS in the film matrix resulted in increased adsorption capacity in the visible region. As a whole, including TiO_2-NPs into the CS network dramatically reduces UV transmission, making them extremely useful for applications that require UV protection, photocatalytic characteristics, and antibacterial effects when exposed to UV light. In the visible range (400-800 nm), the decrease in transmittance as TiO_2-NPs concentration increases may be explained by the possibility of increasing TiO_2-NPs agglomeration, which may prevent light transformation throughout the film due to TiO_2-NPs incorporation into the CS matrix [18,87]. Figure 9c displays the reflectance spectra of the prepared films. The reflectance values declined as the amount of TiO_2-NPs increased. This could be attributed to the inclusion of TiO_2-NPs in the CS network, which resulted in reduced reflection due to the smaller sizes of the nanoparticles relative to the wavelength of visible light, indicating low light scattering ability [28,50].

The opacity and transparency of composite films possess important characteristics, particularly when they are intended for use as food packaging materials. The opacity and transparency of pure CS and CS/TiO2 nanocomposites can be determined using the following relationships [3,18,86]:

$$\text{Opacity} = \frac{A_{600}}{d}, \tag{10}$$

$$\text{Transparency} = \frac{-\log(\%T_{600})}{d}, \tag{11}$$

where A_{600} is the absorbance at 600 nm, $\%T_{600}$ is the percentage transmittance at 600 nm, and d is the film thickness in millimeters. Table 4 presents a comparison of the opacity and transparency values of pure CS and CS/TiO_2 nanocomposites. As noted, the higher the opacity value, the lower the transparency of the film. The opacity value of pure CS film is 1.601 mm^{-1}, which increases considerably as the amount of TiO_2-NPs increases, reaching a maximum of 18.336 mm^{-1} for the CS/12 wt% TiO_2 nanocomposite. Transparency values reduced dramatically from 30.666 to 2.774 mm^{-1} when the concentration of TiO_2-NPs was raised from 0 to 12 wt%. This rise in opacity (reduction in

transparency) values was caused by the interaction of TiO_2-NPs with the CS matrix, which is responsible for the compact and higher polymeric chain network that prevents the passage of UV and visible light. These findings can be explained by the fact that when TiO_2-NPs interacted with CS chains, a discontinuity formed in the CS matrix, resulting in a more disordered structure [3,18,86].

Measurements of optical transmittance (T) and reflectance (R) were utilized to evaluate optical parameters, including absorption coefficient (α), extinction coefficient (K), and refractive index (n). The absorption coefficient (α) is a crucial optical characteristic that determines how far light can travel within a film before absorption. It is also an important parameter for determining the absorption edge, kind of transition, and energy gap. The absorption coefficient of the manufactured films has been calculated using the following formula [88,89]:

$$\alpha = \frac{1}{d} \ln \frac{(1-R)^2}{T}, \tag{12}$$

where d is the thickness of the film.

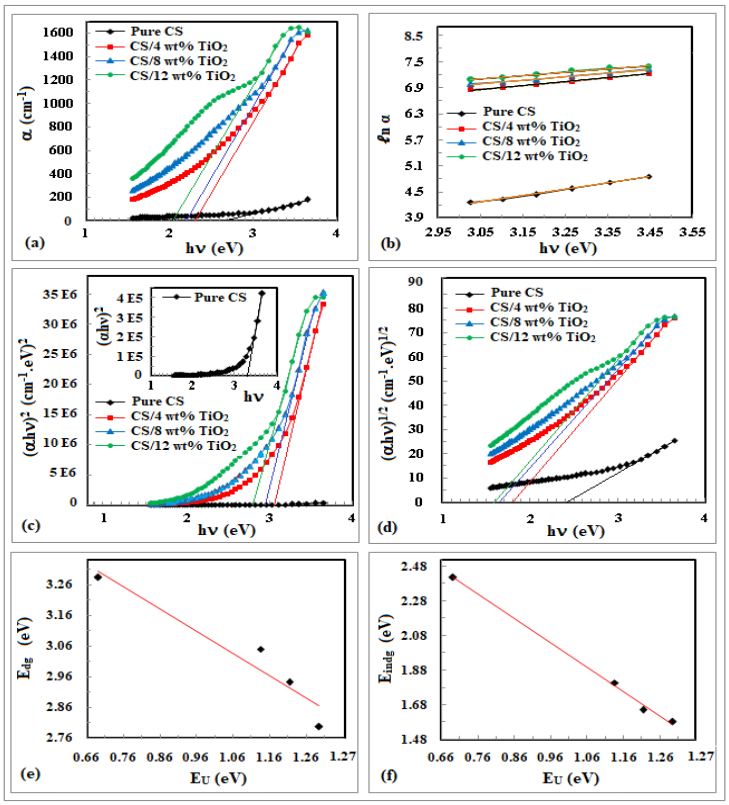

Figure 10. (a) α, (b) ℓn α, (c) $(\alpha h\nu)^2$, and (d) $(\alpha h\nu)^{½}$ against hν; (e) E_U versus E_{dg} and (f) E_U versus E_{indg} for pure CS and CS/TiO_2 nanocomposite films

Figure 10a shows a plot of the absorption coefficient (α) versus incident photon energy (hν) for pure CS and CS/TiO_2 nanocomposite films. Increasing the photon energy and TiO_2-NP concentration to 12 wt% leads to an increase in α value. To calculate the absorption edge (E_{ed}) values, extrapolate the linear parts to α = 0 on the hν-axis and the computed values are listed in Table 4. The E_{ed} value for pure CS was shown to decrease toward lower energy values (higher wavelengths) as the concentration of TiO_2-NPs increased. E_{ed} values decrease from 2.716 to 2.043 eV as the concentration of TiO_2-NPs increases from 0 to 12 wt%. This was closely correlated with the production of charge-transfer complexes in nanocomposite films [21]. The observed decrease in E_{ed} value could be related to the enhancement of the amorphous phase, resulting in changes in the structure of the CS/TiO_2 nanocomposites [8,90]. Further, the decrease in E_{ed} may imply the presence of intra- or inter-molecular interaction between Ti^{4+} ions and neighboring OH groups in the CS matrix [50]. Also, this observation suggests that the electronic polarization values of the nanocomposites change, demonstrating the decrease in the optical energy band gap values and changes occurring in the band structure of the CS/TiO_2 nanocomposites [8,90,91].

The Urbach energy (E_U) describes the order of a matter system by calculating the width of the tail of local states in the forbidden gap. It can be determined using the Urbach empirical formula as follows [92,93]:

$$\ln \alpha = \ln \alpha_o + \frac{h\nu}{E_U}, \tag{13}$$

α_o represents a pre-exponential factor. Figure 10b shows a plot of ℓn α against hν for pure CS and CS/TiO_2 nanocomposites. Table 4 lists the calculated Urbach energy (E_U) values based on the reciprocal slopes of the fitted lines.

The E_U values rise from 0.692 eV for pure CS to 1.295 eV for the CS/12 wt% TiO_2 nanocomposite. This increase in E_U values indicates that a disruption in the band structure occurred, increasing structural disorder and enhancing the amorphous phase of the film. In addition, detailed information on the density of defects (DOF) and relaxation of the distorted bonds can be obtained by computing the steepness parameter (S) and electron-phonon interaction strength ($E_{e\text{-}p}$) using the following relations [92,93]:

$$S = \frac{k_B T}{E_U}, \text{ and } E_{e-p} = \frac{2}{3S}, \tag{14}$$

where k_B and T represent Boltzmann's constant and room temperature (=298 K), respectively. Table 4 gives the computed values for S and $E_{e\text{-}p}$. The steepness parameter (S) values decreased from 0.037 to 0.020, while the electron-phonon interaction strength ($E_{e\text{-}p}$) values increased from 17.929 to 33.583 as the concentration of TiO_2-NPs increased from 0 to 12 wt%. Thus, the inclusion of TiO_2-NPs into the CS network may be responsible for the inverse change between S and $E_{e\text{-}p}$, causing the ionicity and anion valence of the CS/TiO_2 nanocomposite change. Additionally, these variations in S and $E_{e\text{-}p}$ show that the density of defects (DOF) increases around the absorption edge, confirming the improvement of the amorphous phase of CS with increasing TiO_2-NP concentration [8,92,93].

Table 4. Optical parameter values: opacity, transparency, E_{ed}, E_U, S, $E_{e\text{-}p}$, E_{dg}, E_{indg} and N_{cc} of pure CS and CS/TiO_2 nanocomposites

Sample	Opacity (mm^{-1})	Transparency (mm^{-1})	E_{ed} (eV)	E_U (eV)	S	$E_{e\text{-}p}$	E_{dg} (eV)	E_{indg} (eV)	N_{cc}
Pure CS	1.601	30.666	2.716	0.692	0.037	17.929	3.282	2.417	110
CS/4 wt%TiO_2	9.421	17.633	2.303	1.135	0.023	29.428	3.050	1.807	127
CS/8 wt%TiO_2	13.153	11.411	2.206	1.214	0.021	31.463	2.943	1.651	137
CS/12wt%TiO_2	18.336	2.774	2.043	1.295	0.020	33.583	2.798	1.581	151

The energy band gap of a material is determined by its greater absorption spectra (first region), which is strongly influenced by the absorption coefficient (α). Tauc's relation was used to compute the optical energy band gap (E_g) as follows [45,94,95]:

$$(\alpha h\nu)^p = B(h\nu - E_g), \tag{15}$$

where B is a constant known as the band-tailing parameter (Tauc's slope) and p is the power factor that describes the sort of electronic transition. Exponent p can have values of 2 or 1/2, corresponding to direct or indirect allowed transitions, respectively. Figure 10c and d show graphs of $(\alpha h\nu)^2$ and $(\alpha h\nu)^{1/2}$ versus hν for pure CS and CS/TiO_2 nanocomposites, respectively. The direct (E_{dg}) and indirect (E_{indg}) energy band gaps can be calculated by extending the linear portions to $(\alpha h\nu)^2 = 0$ and $(\alpha h\nu)^{1/2} = 0$ on the hν-axis. Table 4 summarizes the computed values of E_{dg} and E_{indg}. As TiO_2-NP concentrations increase, the E_{dg} and E_{indg} values decrease. As the TiO_2-NPs content increases from 0 to 12 wt%, E_{dg} values decrease from 3.282 to 2.798 eV and E_{indg} values decrease from 2.417 to 1.581 eV. The decrease in energy band gap could be due to an excessive amount of localized states in the band structure. These declines in the values of E_{dg} and E_{indg} could be attributed to increased disorder within the nanocomposite film's structure. This disorder creates new vacant energy levels in the band gap, allowing electrons to move more easily between the valence and conduction bands [45].It may also be related to the existence of electronic interaction between TiO_2-NPs and CS polymer, resulting in an increase in absorption intensity [90]. The decreases in E_{ed}, E_{dg} and E_{indg} values of nanocomposite films suggest changes to the CS microstructure and band structure, possibly due to the formation of new optical transition clusters. Figure 10e and f shows the variance of E_{dg} and E_{indg} versus E_U, respectively. The energy band gap reduces as the value of E_U increases, indicating a direct correlation with E_{dg} and E_{indg}. These findings are consistent with previous research, as band gap lowering can lead to the formation of localized states in the optical band gap as a result of defects forming in the CS matrix [93,96]. Using these two approaches, the following linear fitting relationships can be estimated:

$$E_{dg} = 3.804 - 0.725E_U, \tag{16a}$$

$$E_{indg} = 3.391 - 1.409E_U. \tag{16b}$$

It was discovered that increasing the Urbach energy of the film indicates a decrease in the values of the optical energy band gap. This observation supports the assumption that introducing TiO_2-NPs will enhance the number of traps.

The following equation can be used to compute the number of carbon atoms per cluster (N_{cc}) in pure CS and CS/TiO_2 nanocomposites using the direct optical energy band gap (E_{dg}) values [97,98]:

$$N_{cc} = \frac{1.1834 \times 10^3}{E_{dg}^2}. \tag{17}$$

The calculated N_{cc} values are shown in Table 4. The N_{cc} values increased from 110 for pure CS to 151 for the CS/12 wt% TiO_2 nanocomposite. The rise in N_{cc} values may be due to the resultant conjugation between CS matrix monomer units following the incorporation of TiO_2-NPs. This result can be related to the existence of more defects in the CS matrix as the TiO_2-NP content increases, resulting in the formation of additional low energy levels, lowering the optical band gap and improving N_{cc} values. Abdelfattah et al. [8] and Ahmed et al. [98] reported a similar trend. As a result, the observed variations confirm the increasing disorder degree in nanocomposite samples where the optical band

gap is compositionally dependent [97,98]. The decreased energy gap values of CS following the incorporation of TiO_2-NPs make it a promising material for optoelectronic devices. Moreover, based on the results, it is clear that CS/TiO_2 nanocomposites could be used in the design and manufacture of custom packaging materials to block sunlight and prevent the formation of toxic substances, unpleasant odors, and flavors, preserve food color, and prevent photo-oxidation of fats in food products if used as active food packaging materials [28].

Linear optical parameters

Many of the optical parameters that contribute to the effective use of polymeric nanocomposites in a variety of industrial, medical, and optoelectronic applications are directly related to the extinction coefficient (K) and refractive index (n) parameters [8,91,98,106]. The optical parameters K and n were determined to obtain an understanding of the polarization and optical variations in the produced nanocomposite films. The extinction coefficient (K), a parameter that represents the fraction of energy lost as a result of absorbing or scattering due to the interaction between the incident photon and the charge of the medium, can be described as follows [50,90]:

$$K = \frac{\alpha\lambda}{4\pi}. \tag{18}$$

Figure 11a shows the relationship between the extinction coefficient (K) and wavelength (λ) in pure CS and CS/TiO_2 nanocomposites. The behavior of K varied significantly across all nanocomposite samples as compared to the pure CS film. It was demonstrated that K values altered on the order of 10^{-3}. K values in nanocomposite films increase with rising UV wavelengths. This increase in K value reveals that electromagnetic waves cannot pass through this region, which can be explained by the fact that some of the energy was scattered or reflected by these nanocomposites, causing damping and decay. In contrast, as seen in Figure 11a, the K value decreased in the visible range and the extinction coefficient (K) behaves similarly to the absorption coefficient (α); see Figure3a. Furthermore, as noted in Equation 18, K is directly proportional to α, which explains the reduction in values of K as the wavelength increases. On the other hand, increasing the concentration of TiO_2-NPs incorporated into chitosan in the nanocomposite film to 12 wt% resulted in a significant rise in K values as the absorbance of the manufactured nanocomposites was enhanced. This indicates that the extinction coefficient is determined by the defects in structure and free electron densities present in the nanocomposite under consideration. This discovery verifies the results of the transmittance spectra, as well as the previously indicated opacity and transparency values. As a result, the acquired K values show that the manufactured films have no surface imperfections that enhance roughness, making them a good choice for optoelectronic devices [99].

The refractive index reveals how an incoming photon persuades molecules to polarize. The improved design of optoelectronic devices necessitates a thorough examination of the material's refractive index behavior. The refractive index (n) can be determined using Fresnel's relation as follows [14,50]:

$$\mathrm{n} = \frac{1+R}{1-R} + \sqrt{\frac{4R}{(1-R)^2} - K^2}\ . \tag{19}$$

Figure 11b illustrates the relationship between refractive index (n) and wavelength (λ) in pure CS and CS/TiO_2 nanocomposites. It was found that the refractive index decreases significantly in the UV zone while remaining rather steady as the wavelength increases. This unremarkable decrease in the visible region could be explained to the fact that the molecules in the sample do not obey the applied electromagnetic field alternations due to their inertia [87]. Furthermore, increasing the TiO_2-NPs content in the CS matrix reduces the nanocomposite's refractive index values, which can be attributed to a decrease in the free charge carrier concentration and polarizability of the nanocomposite samples [100]. The interaction of TiO_2-NPs with CS molecules may modify the CS refractive index, and the variations in the refractive indices of the film components may affect the film's transparency (opacity) [50].

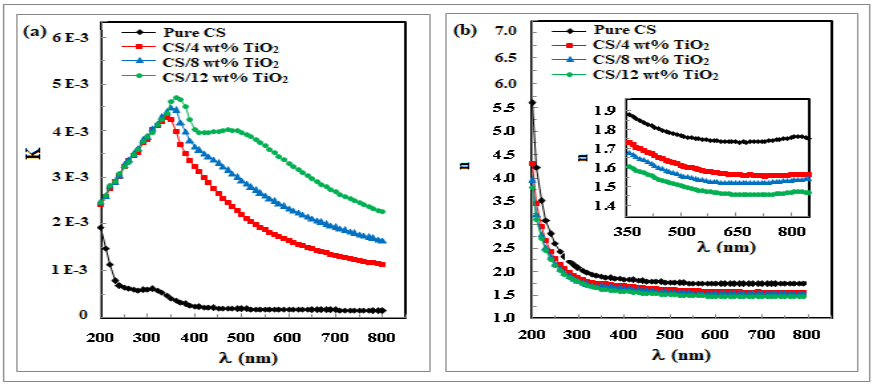

Figure 11. (a) The extinction coefficient, K, and (b) the refractive index, n, versus wavelength, λ, for pure CS and CS/TiO_2 nanocomposite films

Wemple and Di-Domenico dispersion parameters

Dispersion parameters are useful in assessing the optical properties of any material for use in the construction of photoelectronic devices [8,91]. The observed dispersion in the refractive index in Figure 11b can be applied to determine the dispersion energies using the Wemple-DiDomenico model (single-oscillator model). The following relation relates the refractive index (n) and photon energy (hν) [8,92,98,101]:

$$(n^2-1)^{-1} = \frac{E_o}{E_d} - \frac{(h\nu)^2}{E_o E_d}, \tag{20}$$

where E_d is the effective energy of dispersion, which quantifies the average strength of inter-band transitions in the film, and E_o is the single effective oscillator energy (the WDD-gap), which provides quantitative information about the film's overall band structure. Figure 12a displays the graphical relationship between $(n^2-1)^{-1}$ and $(h\nu)^2$ for pure CS and CS/TiO_2 nanocomposites. The WDD parameters (E_d and E_o) can be determined using the $(n^2-1)^{-1}$-axis intercept (E_o/E_d) and the negative slope ($1/E_oE_d$) of the straight line fit, as can be seen in Table 5.The following equations were used to calculate dispersive parameters based on E_d and E_o, such as oscillation field strength (f), Wemple-DiDomenico optical energy band gap (E_g^{WDD}), static refractive index (n_0), and static dielectric constant at infinite wavelength (ε_s) [102,103]:

$$f = E_o E_d, \quad E_g^{WDD} = \frac{E_o}{2}, \quad n_0 = \sqrt{1 + \frac{E_d}{E_o}}, \quad and \quad \varepsilon_S = n_0^2 \tag{21}$$

Table 5 shows the computed oscillator parameters for CS and nanocomposite films. The table demonstrates that the values of E_d, E_o, f, n_0, and ε_s decrease when TiO_2-NPs concentration increases. By increasing the percentage of TiO_2-NPs from 0 to 12 wt%, the E_d values reduce gradually from 11.324 to 5.621 eV, while the E_o values decrease from 6.308 to 5.393 eV, resulting in a decrease in direct band gap energy (E_{dg}) values and being compatible with increases in Urbach energy (E_U). To establish a correlation between direct band gap energy (E_{dg}) and effective oscillator energy (E_o), the table revealed that the ratio $E_o/E_{dg}$was found to be in the range 1.922–1.828 ($E_o \approx 1.9\ E_{dg}$), which coincides with the prediction of the Wemple-DiDomenico model for the current CS and CS/TiO_2 nanocomposite films. This finding in the Eo/Eg ratio shows thermally created defects that produce localized states around energy band gaps, which have a significant impact on the optical characteristics of nanocomposite films [91,92,102]. The table shows that increasing the content of TiO_2-NPs from 0 to 12 wt% reduced the oscillation field strength (f) – f represents the interaction strengths between the material and the electromagnetic radiation – values from 71.429 to 29.412 (eV) ^{2}, indicating a weaker composition of the nanocomposite film. The E_g^{WDD} values decrease from 3.154 to 2.697 eV when the TiO_2-NPs concentration is increased from 0 to 12 wt%, which could be attributable to variations in atom diffusion rates in the nanocomposites and imply that the number of atoms in the previously identified interstitial has altered. The values of E_g^{WDD} are consistent with the values of the direct energy band gap (E_{dg}) (see Table 4). This result suggests that the inclusion of TiO_2-NPs reduces the system's average bonding strength or cohesive energy while increasing the disorder degree in the CS matrix [102,104]. The computed static refractive index (n_0) values decreased from 1.672 to 1.418 as the concentration of TiO_2-NPs increased from 0 to 12 wt%. The static dielectric constant (ε_s) values decreased from 3.642 to 2.702 as the amount of TiO_2-NPs increased from 0 to 12 wt%. These observations could indicate an increase in structural disorder, which alters the optical properties of the film.

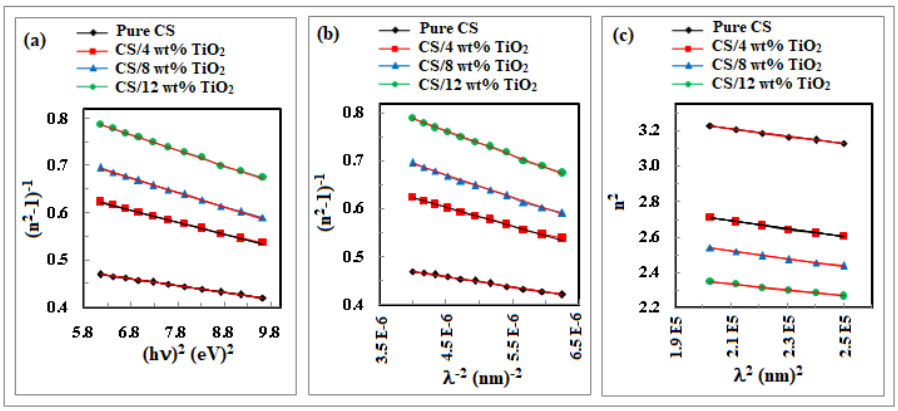

Figure 12. (a) $(n^2-1)^{-1}$ versus $(h\nu)^2$, (b) $(n^2-1)^{-1}$ versus λ^{-2} and (c) n^2 versus λ^2 for pure CS and CS/TiO_2 nanocomposite films

The first optical moment (M_{-1}) and second optical moment (M_{-3}) of CS and CS/TiO_2 nanocomposite films, which measure the process of light-material interaction, were computed using the estimated E_d and E_o values from the following equations [8,98]:

$$M_{-1} = \frac{E_d}{E_o}, \quad and \quad M_{-3} = \frac{M_{-1}}{E_o^2}. \tag{22}$$

Table 5 also included the computed M_{-1} and M_{-3} values for all samples. It has been found that while the transition moments M_{-1} and M_{-3} are mainly determined by the values of E_d and E_o, their values follow similar trends and decrease as the TiO_2-NPs content increases. When the concentration of TiO_2-NPs was increased from 0 to 12 wt%, M_{-1} reduced from 1.795 to 1.011, and M_{-3} decreased from 0.045 to 0.035 $(eV)^{-2}$. This result validates the structural dependency of the optical properties of the nanocomposites under study, as well as the enhancement of the amorphous phase of the CS/TiO_2 nanocomposite [8,98].

Table 5. The evaluatedvalues of E_d, E_o, E_o/E_{dg} ratio, f, E_g^{WDD}, n_0, ε_s, M_{-1}, M_{-3}, λ_o, S_o, ε_L, N/m*, N and ω_p, for pure CS and CS/TiO_2 nanocomposites

Dispersion parameters	Samples			
	Pure CS	CS/4wt% TiO_2	CS/8wt% TiO_2	CS/12wt% TiO_2
E_d (eV)	11.324	7.179	6.148	5.621
E_o (eV)	6.308	5.575	5.422	5.393
E_o/E_{dg} ratio	1.922	1.828	1.842	1.928
f $(eV)^2$	71.429	39.999	33.333	29.412
E_g^{WDD} (eV)	3.154	2.788	2.711	2.697
n_0	1.672	1.512	1.461	1.418
ε_s	2.795	2.287	2.134	2.011
M_{-1}	1.795	1.287	1.134	1.011
M_{-3} $(eV)^{-2}$	0.045	0.041	0.039	0.035
λ_o (m)	1.988×10^{-7}	2.230×10^{-7}	2.307×10^{-7}	2.258×10^{-7}
S_o (m^{-2})	4.541×10^{13}	2.588×10^{13}	2.131×10^{13}	1.982×10^{13}
ε_L	3.642	3.163	2.982	2.702
N/m* $(m^{-3}.kg^{-1})$	8.840×10^{56}	8.789×10^{56}	8.557×10^{56}	7.584×10^{56}
N (m^{-3})	3.543×10^{26}	3.523×10^{26}	3.430×10^{26}	3.040×10^{26}
ω_p (Hz)	1.601×10^{15}	1.596×10^{15}	1.571×10^{15}	1.483×10^{15}

The average oscillator wavelength (λ_o) and average oscillator strength (S_o) were determined using the following Wemple-Didomenico formulae [8,98,101]:

$$(n^2-1)^{-1} = (n_0^2-1)^{-1} - \frac{\lambda_o^2}{(n_0^2-1)}\ \lambda^{-2}, \quad and \quad S_o = \frac{(n_0^2-1)}{\lambda_o^2}. \tag{23}$$

Graphing the relationship between $(n^2-1)^{-1}$ and λ^{-2}yields a negative slope ($-1/S_o$) line that intersects the λ^{-2}-axis at ($1/S_o\lambda_o^2$) (Figure 12b). The parameters λ_o and S_o were computed and shown in Table 5. As TiO_2-NPs concentration increases from 0 to 12 wt%, $\lambda_o$values increase from 198.8 to 225.8 nm, while S_o values decrease from 4.541×10^{13} to 1.982×10^{13} m^{-2}. According to Hassanein [105], λ_o is inversely proportional to E_o, and since E_o is directly proportional to E_g, λ_o will be inversely proportional to E_g. However, S_o is directly proportional to E_d, therefore S_o will be directly proportional to E_g.

The refractive index (n) data can be examined to calculate the lattice dielectric constant at a longer wavelength (ε_L), taking into account dispersion vibrations and free carriers. The following equation represents the relationship between the refractive index (n) and wavelength (λ) [8,98]:

$$n^2 = \varepsilon_L - \frac{e^2}{4\pi\varepsilon_o c^2}\left(\frac{N}{m^*}\right)\lambda^2, \tag{24}$$

where ε_L is the lattice dielectric constant, ε_o is the free space permittivity (= 8.854×10^{-12} $F\cdot m^{-1}$ or $C^2\cdot N^{-1}\cdot m^{-2}$), c is the speed of light in space (= 3×10^8 $m\cdot s^{-1}$), e is the electron charge (= 1.602×10^{-19} C), and (N/m*) is the ratio of charge carrier concentration (N) and effective mass (m*). Figure 12c depicts the graphical representations of n^2 and λ^2 for pure CS and CS/TiO_2 nanocomposites. Table 5 summarizes the calculated ε_L and N/m* values based on the intersection and slope of fitted lines. Assuming m* = 0.44 m_e (m_e is the electron's rest mass = 9.109×10^{-31} kg), the value of N is computed and listed in Table 5. The table reveals that increasing the TiO_2-NPs concentration from 0 to 12 wt% decreases ε_L from 3.642 to 2.702, N/m* ratio from 8.840×10^{56} to 7.584×10^{56} $m^{-3}.kg^{-1}$, and N values from 3.543×10^{26} to 3.040×10^{26} per m^3. Table 5 indicates that ε_s values are lower than ε_L values, possibly due to the polarization process caused by light and decreased charge carrier concentrations [8,106,107].

The plasma frequency (ω_p); corresponds to the typical electrostatic oscillation frequency in response to a small charge separation; of CS and CS/TiO_2 nanocomposite films was calculated using the classical Drude dispersion model and the ratio N/m* as follows [8]:

$$\omega_p = \sqrt{\frac{e^2}{\varepsilon_o}.\frac{N}{m^*}}. \tag{25}$$

Table 5 lists the computed ω_p values. Increasing TiO_2-NPs content from 0 to 12 wt% causes a decrease in ω_p values from 1.601×10^{15} to 1.483×10^{15} Hz. High ω_p values were attributed to high free carrier concentrations, as ω_p is mainly determined by charge carrier concentration (N). Adding more TiO_2-NPs reduces the time-variation of the electric field caused by resonance effects, resulting in lower frequency values [98,105].

Nonlinear optical parameters

The study of nonlinear optical properties of materials such as nanocomposites is crucial for predicting their ability to be used in a wide range of optical applications, including internet access, optical regulators, optical networks, optical switching equipments and frequency conversion devices [8,93,102]. The nonlinear optical polarizability (P) within the material was obtained by expanding the power sequence of the entire applied optical field (E) [8,93]:

$$P = \chi^{(1)}E + \chi^{(2)}E^2 + \chi^{(3)}E^3 + \ldots\ldots \tag{26}$$

where $\chi^{(1)}$ is the first-order linear susceptibility, $\chi^{(2)}$ is the second-order nonlinear susceptibility, and $\chi^{(3)}$ is the third-order nonlinear optical susceptibility. The following semi-empirical relation was used to calculate the first-order linear susceptibility ($\chi^{(1)}$) based on the linear refractive index (n) [12,95]:

$$\chi^{(1)} = \frac{(n^2-1)}{4\pi} \quad . \tag{27}$$

Using WDD-dispersion energies (E_d and E_o) and Equation 20, $\chi^{(1)}$ can be expressed as:

$$\chi^{(1)} = \frac{E_o E_d}{4\pi\ [E_o^2 - (h\nu)^2]} \quad . \tag{28}$$

At the limit $h\nu \rightarrow 0$ ($n = n_0$), using Equations 27 and 28 one obtains:

$$\chi^{(1)} = \frac{(n_0^2-1)}{4\pi} = \frac{E_d}{4\pi E_o}. \tag{29}$$

The nonlinear optical (NLO) properties of a material are expressed by its third-order nonlinear susceptibility ($\chi^{(3)}$) and nonlinear refractive index (n_2). According to Miller's principle and WDD model, $\chi^{(3)}$ can be approximated using the following expression [14,95,102]:

$$\chi^{(3)} = A\left(\chi^{(1)}\right)^4, \tag{30}$$

where A is a constant factor independent of photon energy (about 1.7×10^{-10}esu for all materials). For $h\nu \rightarrow 0$, $\chi^{(3)}$ can be expressed as:

$$\chi^{(3)}(esu) = A\left(\frac{n_0^2-1}{4\pi}\right)^4 = 6.8\times10^{-15}\left(\frac{E_d}{E_o}\right)^4. \tag{31}$$

The nonlinear refractive index (n_2) and nonlinear absorption coefficient (β_c) were calculated using the following equations [12,98,102]:

$$n_2 = \frac{12\pi\chi^{(3)}}{n_0}, \tag{32}$$

$$\beta_c = \frac{48\pi^3\chi^{(3)}}{n^2 c\lambda}. \tag{33}$$

Figure 13a-d shows the spectrum distributions of $\chi^{(1)}$, $\chi^{(3)}$, n_2, and β_c versus wavelength (λ) for pure CS and CS/TiO_2 nanocomposites, respectively. The values of $\chi^{(1)}$, $\chi^{(3)}$, n_2, and β_c decrease dramatically with increasing wavelength (decreasing photon energy) and TiO_2-NP concentration. As the percentage weight of TiO_2-NPs increased, the refractive index (n) decreased, resulting in decreases in $\chi^{(1)}$, $\chi^{(3)}$, n_2, and β_c values. This suggests that using a higher concentration of TiO_2-NPs may help to change the local polarization and reduce the number of free charge carriers in the nanocomposite film. Table 6 gives the computed values of $\chi^{(1)}$, $\chi^{(3)}$, and n_2 at $h\nu \rightarrow 0$, for pure CS and CS/TiO_2 nanocomposites. The predicted value of $\chi^{(1)}$ decreases from 0.143 for the pure CS sample to 0.080 for the CS/12 wt% TiO_2-NP nanocomposite. The table shows a significant decrease in $\chi^{(3)}$ values from 70.826×10^{-15}esu for pure CS to 7.126×10^{-15} esu for a CS/12 wt% TiO_2-NPs nanocomposite, which is strongly associated with other parameters. As TiO_2-NPs concentration increased from 0 to 12 wt%, n_2 values reduced from 15.970×10^{-13} to 1.894×10^{-13} esu. The reduction in n_2 values supports the decrease in static refractive index (n_0) values of the CS/TiO_2 nanocomposite samples as the TiO_2-NP concentration increases. The observed changes in susceptibility and nonlinear index of refraction values were considered to be caused by variations in the samples' band gap values and densities. Because n_2 values are on the order of 10^{-12}-10^{-13}, intense light beams were required to make a substantial influence. The acquired results revealed a

substantial association with the other linear parameters evaluated for the prepared samples. The nonlinear parameter results show that the investigated CS/TiO_2 nanocomposites can serve as a good advancer in a variety of optical applications [8,98,109].

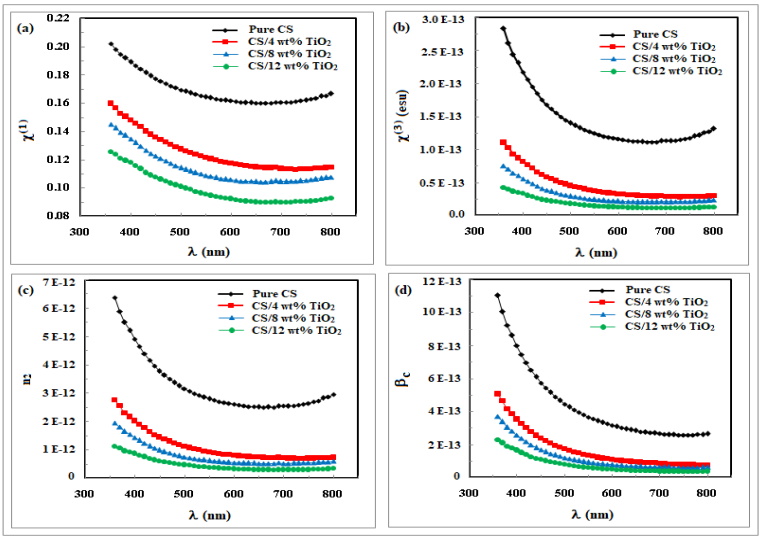

Figure 13. Plots of: (a) $\chi^{(1)}$ and (b) $\chi^{(3)}$ against hv; (c) n_2 and (d) β_c versus λ, for pure CS and CS/TiO_2 nanocomposite films

Table 6. Values of $\chi^{(1)}$, $\chi^{(3)}$, and $n_2$for pure CS and CS/TiO_2 nanocomposites

Dispersion parameters	**Samples**			
	Pure CS	**CS/4 wt% TiO_2**	**CS/8 wt% TiO_2**	**CS/12 wt% TiO_2**
$\chi^{(1)}$	0.143	0.102	0.090	0.081
$\chi^{(3)}$ (esu)	70.826×10^{-15}	18.704×10^{-15}	11.265×10^{-15}	7.126×10^{-15}
n_2 (esu)	15.970×10^{-13}	4.663×10^{-13}	2.907×10^{-13}	1.894×10^{-13}

Optical dielectric constants and optical conductivities

When a material is electronically activated by UV-Vis radiation, the optical dielectric constant can be explained using the electronic excitation spectrum of any material [84,98,98]. The complex dielectric constant (ε*) and its components [real part (ε_r) and imaginary part (ε_i)] represent the decrease in the speed of light and the absorption energy of the electric field caused by the dipole movement of molecules in films. The complex dielectric constant (ε*) and its components (ε_r and ε_i) can be calculated using the refractive index (n) and extinction coefficient (K) data as follows [93,98]:

$$\varepsilon^* = \varepsilon_r + i\,\varepsilon_i, \quad \varepsilon_r = n^2 - K^2 \;\; and \;\; \varepsilon_i = 2nK\,. \tag{34}$$

Figure 14 shows how the real, ε_r (a) and imaginary, ε_i (b) dielectric constants for pure CS and CS/TiO_2 nanocomposites vary with wavelength (λ). As demonstrated in Figure 14a, ε_r increased with photon energy, corresponding to the behavior of the refractive index (see Figure 11b). The polar nature of CS/TiO_2 nanocomposites causes fluctuations in the incident electromagnetic wave field, resulting in a dispersion region in the photon energy range of 3.6–6.2 eV (<350 nm) for all samples. The observed higher ε_r values were attributable to the high contribution of the free charge carrier. The spectra, on the other hand, tend to behave consistently at lower photon energies (i.e., in the visible region). Due to inertia, molecules in this region are unable to follow oscillations in the incident field, resulting in nearly constant ε_r values. The dispersion region of a nanocomposite plays an important role for optical networking and device design, as the real dielectric constant (ε_r) affects electron mobility during light transformation and slows photon propagation. Figure14a shows that when the amount of TiO_2-NPs in the nanocomposite film of the CS matrix increased, the values of ε_r decreased. This indicates that the incorporation of TiO_2-NPs into the CS/TiO_2 nanocomposite enhanced the energy dissipative and disruptive rates of incident light on the film, indicating a reduction in the speed of light propagation within the films. The imaginary dielectric constant part (ε_i) reflects energy absorption from dipole motion and measures the disruptive rate of light waves through the material. Figure 14b indicates that ε_i values steadily increase in the visible region as photon energy and TiO_2-NPs content increase. The variance in ε_i values was related to the dipolar polarization of the nanocomposite [108]. Because of the direct relationship between ε_i and K, the trend of ε_i in prepared films mimics the behavior of K. Additionally, Figure 14a and b shows that ε_r values are significantly higher than ε_i. The discrepancy in ε_r and $\varepsilon_i$values indicates interactions between free electrons and photons in the nanocomposite films under investigation. Furthermore, the observed differences in the optical dielectric constant values of the CS/TiO_2 nanocomposite samples compared to pure CS verify the presence of more density of states (DOS), resulting in increased polarization and higher dielectric constant values [90,98].

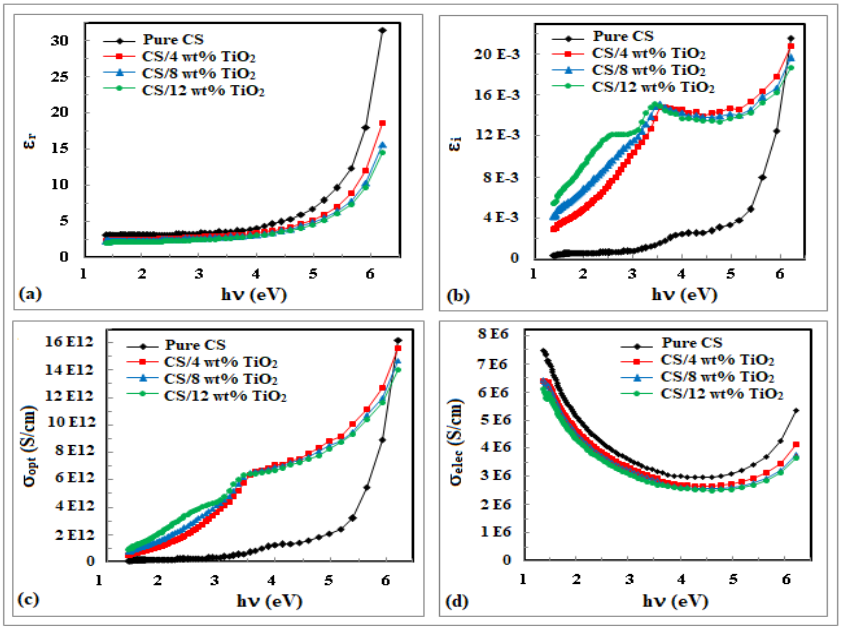

Figure 14. Plots of: (a) ε_r , (b) ε_i , (c) σ_{opt}, and (d) σ_{elec} against hν for pure CS and CS/TiO_2 nanocomposite films

The optical and electrical conductivities of the manufactured films were determined in order to understand more about their optical response. The optical (σ_{opt}) and electric (σ_{elec}) conductivities of the produced films were estimated using the following equations [93,102]:

$$\sigma_{opt} = \frac{\alpha nc}{4\pi}, \quad \text{and} \quad \sigma_{elec} = \frac{2\lambda\sigma_{opt}}{\alpha}. \tag{35}$$

Figure 14 displays graphs of σ_{opt} (c) and σ_{elec}(d) versus photon energy (hν). It was found that both σ_{opt} and σ_{elec} behave differently. Figure 14c shows that increasing the photon energy and TiO_2-NPs content in the CS/TiO_2 nanocomposite improves the σ_{opt} of the films. Additionally, the spectral behavior of σ_{opt} in the films is comparable to that of ε_i (Figure 14b).

High photon energy (low wavelength) in the UV range causes a dramatic increase in σ_{opt} for all films, indicating a strong interaction between charge carriers and energetic photons. In addition, nanocomposite films exhibit higher optical conductivity and absorbance than pure CS film. The produced nanocomposites exhibit high photoresponsiveness, with σ_{opt} values of the order of 10^{12}. This suggests that the band gap has decreased while conductivity increased, indicating that the composite film has a longer conjugation length. This finding indicates that the concentration of charge carriers in the CS/TiO_2 nanocomposites has increased, as well as the enhancement of electron excitation due to an increase in film absorption coefficients and incident photon energy [98,102]. Figure 14d reveals that the electrical conductivity (σ_{elec}) values of the samples are on the order of 10^6. σ_{elec} values decrease with increasing photon energy up to ~4.1 eV (~300 nm), then increase with increasing photon energy to ~6.2 eV (~200 nm). Furthermore, increasing the concentration of TiO_2-NPs in the nanocomposite film to 12 wt% reduces σ_{elec} values. This observed behavior could be attributed to the variance in charge carriers generated by the rising amount of TiO_2-NPs in the produced nanocomposite. The results for optical and electrical conductivities were matched, indicating potential for optical applications.

4. CONCLUSION

In the current study, innovative pure chitosan and chitosan/TiO_2 nanocomposite thin films with differed TiO_2-NP concentrations (4, 8, and 12 wt%) were successfully created applying the solution casting method. The produced films were analyzed using FTIR, thermal analysis, and UV-Vis optical spectroscopy methods. FTIR examination confirmed that there is an interaction between CS and TiO_2-NPs, as well as alterations in the structure of CS caused by the presence of TiO_2-NPs. These changes were observed in the intensities and positions of the absorption peaks of CS/TiO_2 nanocomposites as compared to the pure CS sample. Analysis of DSC data revealed that when the amount of TiO_2-NPs increased, there was an intense interaction between the –OH groups of CS and TiO_2 nanoparticles, confirming the miscibility of the nanocomposites. TGA and DTGA results showed that increasing TiO_2-NP concentrations increased the thermal stability of the nanocomposite due to chemical interactions between the CS-polymer and TiO_2-NPs. Spectroscopy was used to investigate the linear and nonlinear optical properties of pure CS and CS/TiO_2 nanocomposites films in the UV-Vis range between 200 and 800 nm. According to the data, all of the nanocomposite films contain UV-blocking characteristics that are below 360 nm, making them ideal UV light barriers. The Tauck equation and the Urbach postulate were used to calculate the allowed energy band gaps, both direct (E_{dg}) and indirect

(E_{indg}), as well as the Urbach energy (E_U). The absorption edge values (E_{ed}) of the CS/12 wt% TiO_2 nanocomposite were determined to be 2.043 eV, less than 2.716 eV for pure CS. The E_{dg} values reduced dramatically from 3.282 eV for pure CS to 2.798 eV for the CS/12 wt% TiO_2 nanocomposite. E_{indg} values decreased from 2.417 to 1.581 eV when the TiO_2-NPs content increased from 0 to 12 wt%. E_U values increased from 0.692 to 1.295 eV as TiO_2-NP concentrations increased from 0 to 12 wt%. The observed alterations in E_{ed}, E_{dg}, E_{indg}, E_U, S, $E_{e\text{-}p}$, and N_{cc} might be attributed to internal domain differences caused by structure disorder and a decrease in the crystallinity degree of CS. These changes can alter the overall number of potential states. Furthermore, the decrease in direct and indirect energy band gaps was explained in terms of localized states and defects, as confirmed by the Urbach energy. Increasing the concentration of TiO_2-NPs in CS nanocomposite significantly improved optical parameters such as extinction coefficient (K), refractive index (n), real (ε_r) and imaginary (ε_i) optical dielectric constant parts, and optical and electrical conductivities (σ_{opt} and σ_{elec}). In addition, the dispersion properties of the nanocomposites were investigated using the theoretical single oscillator model. The nanocomposites' both nonlinear and linear properties [$\chi^{(1)}$, $\chi^{(3)}$, n_2 and β_c] were increased. The observed innovative results of the linear and nonlinear optical characteristics of the examined nanocomposites indicate that CS/TiO_2 nanocomposite films are promising materials for further investigation for usage as packaging materials for food and in a variety of applications involving optical electronics.

ORCID

Osiris W. Guirguis, https://orcid.org/0000-0003-3670-2904

REFERENCES

[1] Y. Kamari, and M. Ghiaci, "Preparation and characterization of ibuprofen/modified chitosan/TiO_2 hybrid composite as a controlled drug-delivery system", Microporous and Mesoporous Mater. **234**, 361–369 (2016). https://doi.org/10.1016/j.micromeso.2016.07.030

[2] S. Kumar, K. Prasad, J.M. Gil, A.J.F.N. Sobral, and J. Koh,"Mesoporous zeolite-chitosan composite for enhanced capture and catalytic activity in chemical fixation of CO_2", Carbohydr. Polym. **198**, 401–406 (2018). https://doi.org/10.1016/j.carbpol.2018.06.100

[3] V.G.L. Souza, A.L. Fernando, J.R.A. Pires, P.F. Rodrigues, A.A.S. Lopes, and F.M.B., Fernandes, "Physical properties of chitosan films incorporated with natural antioxidants", Ind. Crop. Prod. **107**, 565–572 (2017). http://dx.doi.org/10.1016/j.indcrop.2017.04.056

[4] J. Salvada, B. Alke, C. Brazinha, V.D. Alves, and I.M. Coelhoso,"Development and characterisation of arabinoxylan-based composite films", Coatings, **12**, 813 (2022). https://doi.org/10.3390/coatings12060813

[5] Y. Xing, X. Li, X. Guo, W. Li, J. Chen, Q. Liu, Q. Xu, Q. Wang, H. Yang, Y. Shui, and X. Bi, "Effects of different TiO_2 nanoparticles concentrations on the physical and antibacterial activities of chitosan-based coating film", Nanomaterials **10**, 1365 (2020). https://doi.org/10.3390/nano10071365

[6] V.-B. Hoa, D.-H. Song, K.-H. Seol, S.-M. Kang, H.-W. Kim, J.-H., Kim, S.-S. Moon, and S.-H. Cho, "Application of a newly developed chitosan/oleic acid edible coating for extending shelf-life of fresh pork", Foods, **11**, 1978 (2022). https://doi.org/10.3390/foods11131978

[7] S.B. Aziz, M.M. Nofal, H.O. Ghareeb, E.M.A. Dannoun, S.A., Hussen, J.M. Hadi, K.K. Ahmed, and A.M. Hussein, "Characteristics of poly(vinyl alcohol) (PVA) based composites integrated with green synthesized Al^{3+}-metal complex: structural, optical, and localized density of state analysis", Polymers, **13**, 1316 (2021). https://doi.org/10.3390/polym13081316

[8] E.M. Abdelfattah, H. Elzanaty, W.B. Elsharkawy, M.A. Azzam, Z.M. Elqahtani, S. Alotibi, M. Alyami, and T. Fahmy, "Enhancement of the structure, thermal, linear/nonlinear optical properties, and antibacterial activity of poly(vinyl alcohol)/chitosan/ZnO nanocomposites for eco-friendly applications", Polymers, **15**, 4282 (2023). https://www.mdpi.com/journal/polymers

[9] A. Nešić, G. Cabrera-Barjas, S. Dimitrijević-Branković, S. Davidović, N. Radovanović, and C. Delattre, "Prospect of polysaccharidebased materials as advanced food packaging", Molecules, **25**, 135 (2020). https://doi.org/10.3390/molecules25010135

[10] T.M. Vieira, M., Moldão-Martins, and V.D. Alves,"Design of chitosan and alginate emulsion-based formulations for the production of monolayer crosslinked edible films and coatings", Foods, **10**, 1654 (2021). https://doi.org/10.3390/foods10071654

[11] R.A. Ilyas, H.A. Aisyah, A.H. Nordin, N. Ngadi, M.Y.M. Zuhri, M.R.M. Asyraf, S.M. Sapuan, E.S. Zainudin, S. Sharma, H. Abral, M. Asrofi, E. Syafri, N.H. Sari, M. Rafidah, S.Z.S. Zakaria, M.R. Razman, N. Abd Majid, Z. Ramli, A. Azmi, S.P. Bangar, and R. Ibrahim, "Natural-fiber-reinforced chitosan, chitosan blends and their nanocomposites for various advanced applications", Polymers, **14**, 874 (2022). https://doi.org/10.3390/polym14050874

[12] E.F.M. El-Zaidia, M.S. Al-Kotb, and I.S. Yahia, "Deposition of nanostructured methyl violet-10B films/FTO: Optical limiting and optical linearity/nonlinearity", Mater. Chem. Phys. **240**, 122074 (2020). https://doi.org/10.1016/j.matchemphys.2019.122074

[13] M.V. Vijisha, V.V. Sini, N.K. Siji Narendran, and K. Chandrasekharan, "Enhanced nonlinear optical response from dihydroxy(5,10,15,20-tetraphenyl porphyrinato)tin(IV) or SnTPP in a fully plastic photonic crystal microcavity", Phys. Chem. Chem. Phys. **19**, 29641–29646 (2017). https://doi.org/10.1039/C7CP06455A

[14] M. Yaseen, Z. Farooq, M. Ahmad, M. Abdullah Sultan, M.A. Raza, J.-Y. Winum, M. Mustafa, M.H.R. Mahmood, M. Tayyab, M.A. Iqbal, and M.S. Mahr, "Synthesis and investigation of linear and nonlinear optical properties of an octahedral metalloporphyrin", Opt. Mater. **149**, 115092 (2024). https://doi.org/10.1016/j.optmat.2024.115092

[15] M.A. Neves, J. Hashemi, T. Yoshino, K. Uemura, and M. Nakajima, "Development and characterization of chitosan-nanoclay composite films for enhanced gas barrier and mechanical properties", J. Food Sci. Nutr. **2**, 100007 (2016). https://www.researchgate.net/publication/299488601

[16] G. Xiao, X. Zhang, W. Zhang, S. Zhang, H. Su, and T. Tan, "Visible-light-mediated synergistic photocatalytic antimicrobial effects and mechanism of Ag-nanoparticles@chitosan-TiO_2 organic-inorganic composites for water disinfection", Appl. Catal. B, **170**, 255–262 (2015). https://doi.org/10.1016/j.apcatb.2015.01.042
[17] P. Kaewklin, U. Siripatrawan, A. Suwanagul, and Y.S. Lee, "Active packaging from chitosan-titanium dioxide nanocomposite film for prolonging storage life of tomato fruit", Biol. Macromol. **112**, 523–529 (2018). https://doi.org/10.1016/j.ijbiomac.2018.01.124
[18] H. Haghighi, S. Biard, F. Bigi, R. De Leo, E. Bedin, F. Pfeifer, H.W. Siesler, F. Licciardello, and A. Pulvirenti, "Comprehensive characterization of active chitosan-gelatin blend films enriched with different essential oils", Food Hydrocoll. **95**, 33–42 (2019). https://doi.org/10.1016/j.foodhyd.2019.04.019
[19] S. Yadav, G.K. Mehrotra, P. Bhartiya, A. Singh, and P.K. Dutta, "Preparation, physicochemical and biological evaluation of quercetin-based chitosan-gelatin film for food packaging", Carbohydr. Polym. **227**, 115348 (2020). https://doi.org/10.1016/j.carbpol.2019.115348
[20] M. Islam, S. Masum, M.M. Rahman, A.I. Molla, A.A. Shaikh, and S.K. Roy, "Preparation of chitosan from shrimp shell and investigation of its properties", Int. J. Basic Appl. Sci. **11**, 116–130 (2011).
[21] S.B. Aziz, O.Gh. Abdullah, and M.A. Rasheed, "A novel polymer composite with a small optical band gap: New approaches for photonics and optoelectronics", J. Appl. Polym. Sci. **134**, 44847 (2017). https://doi.org/10.1002/app.44847
[22] S.F. Hamza, M.M. El-Sawy, N.A. Alian, and N.O. Shaker, "Synthesis and evaluation of performance characteristics green composites from sustainable fatty chitosan graft copolymer with acrylic acid for wastewater treatment", Egypt. J. Chem. **64**, 6007–6015 (2021). https://doi.org/10.21608/EJCHEM.2021.73857.3656
[23] Q. Cao, Y. Zhang, W. Chen, X. Meng, and B. Liu, "Hydrophobicity and physicochemical properties of agarose film as affected by chitosan addition", Int. J. Biol. Macromol. **106**, 1307–1313 (2018). https://doi.org/10.1016/j.ijbiomac.2017.08.134
[24] S. Mafirad, M.R. Mehrnia, P. Zahedi, and S.-N. Hosseini, "Chitosan-based nanocomposite membranes with improved properties: Effect of cellulose acetate blending and TiO_2 nanoparticles incorporation", Polym. Compos. **39**, 4452-4466 (2018). https://doi.org/10.1002/pc.24539
[25] M. Mujtaba, R.E. Morsi, G. Kerch, M.Z. Elsabee, M. Kaya, J. Labidi, and K.M. Khawar, "Current advancements in chitosan-based film production for food technology; A review", Int. J. Biol. Macromol. **121**, 889–904 (2019). https://doi.org/10.1016/j.ijbiomac.2018.10.109
[26] M.E. Ergun, E. Ozen, N. Yildirim, B. Dalkilic, and E. Baysal, "Mechanical and thermal properties of polyvinyl acetate foams reinforced with biopolymers", Cell. Polym. **42**, 156–173 (2023). https://doi.org/10.1177/02624893231193501
[27] Z. Hu, P. Hong, M. Liao, S. Kong, N. Huang, C. Ou, and S. Li, "Preparation and characterization of chitosan-agarose composite films", Materials, **9**, 816 (2016). https://doi.org/10.3390/ma9100816
[28] X. Zhang, G. Xiao, Y. Wang, Y. Zhao, H. Su, and T. Tan, "Preparation of chitosan-TiO_2 composite film with efficient antimicrobial activities under visible light for food packaging applications", Carbohydr. Polym. **169**, 101–107 (2017). http://dx.doi.org/10.1016/j.carbpol.2017.03.073
[29] B. Cheba, "Chitosan: Properties, modifications and food nanobiotechnology", Procedia Manuf. **46**, 652–665 (2020). https://doi.org/10.1016/j.promfg.2020.03.093
[30] S.F. Hamza, N.A. Alian, M.M. Elsawy, and N. Shaker, "Preparation, characterization and amtimicrobial activity of chitosan-fatty acid derivatives as a drug delivery system: intercelation and in vitro release of ciprofloxacin", Al-Azhar Bull. Sci. **32**, 47-56 (2021). https://doi.org/10.21608/absb.2021.72129.1110
[31] M.S. Hanafy, W.M. Desoky, E.M. Hussein, N.H. El-Shaer, M. Gomaa, A.A. Gamal, M.A. Esawy, and O.W. Guirguis, "Biological applications study of bio-nanocomposites based on chitosan/TiO_2 nanoparticles polymeric films modified by oleic acid", J. Biomed. Mater. Res. **109**, 232–247 (2021). doi:10.1002/jbm.a.37019
[32] M. Bajić, T.Ročnik, A. Oberlintner, F. Scognamiglio, U. Novak, and B. Likozar, "Natural plant extracts as active components in chitosan-based films: A comparative study", Food Packag. Shelf Life, **21**, 100365 (2019). https://doi.org/10.1016/j.fpsl.2019.100365
[33] B. Tian, and Y. Liu, "Chitosan-based biomaterials: From discovery to food application", Polym. Adv. Technol. **31**, 2408–2421 (2020). https://doi.org/10.1002/pat.5010
[34] S. Moradi, H. Hamedi, A.E. Tonelli, and M.W. King, "Chitosan/graphene oxide composite films and their biomedical and drug delivery applications: A review", Appl. Sci. **11**, 7776 (2021). https://doi.org/10.3390/app11177776
[35] S.M. Bashir, G.A. Rather, A. Patrício, Z. Haq, A.A. Sheikh, M.Z.H. Shah, H. Singh, A.A. Khan, S. Imtiyaz, S.B. Ahmad, S. Nabi, R. Rakhshan, S. Hassan, and P. Fonte, "Chitosan nanoparticles: A versatile platform for biomedical applications", Materials, **15**, 6521–6529 (2022). https://doi.org/10.3390/ma15196521
[36] K. Pieklarz, and K.Modrzejewska, "SARS-CoV-2 – The latest global threat and the prospect of COVID-19 therapy with the use of chitosan",Prog. Chem. Appl. Chitin Deriv. **26**, 41–60 (2021).
[37] S. Valizadeh, M. Naseri, S. Babaei, S.M.H. Hosseini, and A. Imani, "Development of bioactive composite films from chitosan and carboxymethyl cellulose using glutaraldehyde, cinnamon essential oil and oleic acid", Int. J. Biol. Macromol. **134**, 604-612 (2019). https://doi.org/10.1016/j.ijbiomac.2019.05.071
[38] L.A.M. van den Broek, R.J.I. Knoop, F.H.J. Kappen, and C.G. Boeriu, "Chitosan films and blends for packaging material", Carbohydr. Polym. **116**, 237–242 (2015). https://doi.org/10.1016/j.carbpol.2014.07.039
[39] E. Le Goué, C. Gardrat, M. Romain, M. Rollini, C.Moresoli, and V. Coma, "Effect of oleic acid on the release of tetrahydrocurcumin in chitosan-based films", Food Hydrocoll. **124**, 107202 (2022). https://doi.org/10.1016/j.foodhyd.2021.107202
[40] K.S. Siddiqi, A. Rahman, Tajuddin, and A. Husen, "Biogenic fabrication of iron/iron oxide nanoparticles and their application", Nanoscale Res. Lett. **11**, 498 (2016). https://doi.org/10.1186/s11671-016-1714-0
[41] K.S. Siddiqi, and A. Husen, "Recent advances in plant-mediated engineered gold nanoparticles and their application in biological system", J. Trace Elements Med. Biol. 40, 10–23 (2017). https://doi.org/10.1016/j.jtemb.2016.11.012

[42] I. Khan, K. Saeed, andI. Khan, "Nanoparticles: Properties, applications and toxicities", Arab. J. Chem. **12**, 908–931 (2019). https://doi.org/10.1016/j.arabjc.2017.05.011
[43] F. Mohammad, H.A. Al-Lohedan, and H.N. Al-Haque, "Chitosan-mediated fabrication of metal nanocomposites for enhanced biomedical applications", Adv. Mater. Lett. **8**, 89-100 (2017). https://doi.org/10.5185/amlett.2017.6925
[44] K.S. Siddiqi, A. Husen, and R.A.K. Rao, "A review on biosynthesis of silver nanoparticles and their biocidal properties", J. Nanobiotechnol. **16**, 14 (2018). https://doi.org/10.1186/s12951-018-0334-5
[45] F. Gami, N. Algethami, H.M. Ragab, A. Rajah, and A.E. Tarabiah, "Structural, optical and electrical studies of chitosan/polyacrylamide blend filled with synthesized selenium nanoparticles", J. Mol. Struct. **1257**, 132631 (2022). https://doi.org/10.1016/j.molstruc.2022.132631
[46] S. Sau, and S. Kundu, "Variation in structure and properties of poly(vinyl alcohol) (PVA) film in the presence of silver nanoparticles grown under heat treatment", J. Mol. Struct. **1250**, 131699 (2022). https://doi.org/10.1016/j.molstruc.2021.131699
[47] N.R. Saha, G. Sarkar, I. Roy, D. Rana, A. Bhattacharyya, A. Adhikari, A. Mukhopadhyay, and D. Chattopadhyay, "Studies on methylcellulose/pectin/montmorillonite nanocomposite films and their application possibilities", Carbohydr. Polym. **136**, 1218–1227 (2016). https://doi.org/10.1016/j.carbpol.2015.10.046
[48] M. Yang, Y. Xia, Y. Wang, X. Zhao, Z. Xue, F. Quan, C. Geng, and Z. Zhao, "Preparation and property investigation of crosslinked alginate/silicon dioxide nanocomposite films", J. Appl. Polym. Sci. **133**, 43489 (2016). https://doi.org/10.1002/app.43489
[49] W. Ma, J. Li, Y. Liu, X. Ren, Z.G. Gu, Z. Xie, and J. Liang, "Preparation and characterization of excellent antibacterial TiO_2/N-halamines nanoparticles", Colloids Surf. A Physicochem. Eng. Asp. **506**, 284–290 (2016). https://doi.org/10.1016/j.colsurfa.2016.06.055
[50] E.M. Hussein, W.M. Desoky, M.F. Hanafy, and O.W. Guirguis, "Effect of TiO_2 nanoparticles on the structural configurations and thermal, mechanical, and optical properties of chitosan/TiO_2 nanoparticle composites", J. Phys. Chem. Solids, **152**, 109983 (2021). https://doi.org/10.1016/j.jpcs.2021.109983
[51] L.M. Anaya-Esparza, J.M. Ruvalcaba-Gómez, C.I. Maytorena-Verdugo, N. González-Silva, R. Romero-Toledo, S. Aguilera-Aguirre, A. Pérez-Larios, and A.E. Montalvo-González, "Chitosan-TiO_2: A versatilehybrid composite", Materials, **13**, 811 (2020). https://doi.org/10.3390/ma13040811
[52] V.K. Yemmireddy, G.D. Farrell, and Y.C. Hung, "Development of titanium dioxide (TiO_2) nanocoatings on food contact surfaces and method to evaluate their durability and photocatalytic bactericidal property", J. Food Sci. **80**, 1903–1911 (2015). https://doi.org/10.1111/1750-3841.12962
[53] S.A. Oleyaei, H. Almasi, B. Ghanbarzadeh, and A.A. Moayedi, "Synergistic reinforcing effect of TiO_2 and montmorillonite on potato starch nanocomposite films: Thermal, mechanical and barrier properties", Carbohydr. Polym. **152**, 253–262 (2016). https://doi.org/10.1016/j.carbpol.2016.07.040
[54] A. Khalilnezhad, H. Rezvani, P. Ganji, and Y. Kazemzadeh, "A Complete experimental study of oil/water interfacial properties in the presence of TiO_2 nanoparticles and different ions", Oil Gas Sci. Technol. **74**, 39 (2019). https://doi.org/10.2516/ogst/2019007
[55] Q. Chen, Z. Ye, L. Tang, T. Wu, Q. Jiang, and N. Lai, "Synthesis and solution properties of a novel hyperbranched polymer based on chitosan for enhanced oil recovery", Polymers, **12**, 2130 (2020). https://doi.org/10.3390/polym12092130
[56] G.S. Negi, S.Anirbid, and P. Sivakumar, "Applications of silica and titanium dioxide nanoparticles in enhanced oil recovery: Promises and challenges", Petroleum Res. B, 224–246 (2021). https://doi.org/10.1016/j.ptlrs.2021.03.001
[57] A.D. Dos Santos Francisco, K.C.B. Maia, J.G. Vieira Moura, R.S. Veiga Nascimento, F. da Silva Lima, and D. Grasseschi, "Chitosan derivatives as surfactant carriers for enhanced oil recovery – Experimental and molecular dynamic evaluations of polymer-surfactant interactions", Colloids Surf. A Physicochem. Eng. Asp. **671**, 131644 (2023). https://doi.org/10.1016/j.colsurfa.2023.131644
[58] Y.H. Yun, J.W. Yun, S.D. Yoon, and H.S. Byun, "Physical properties and photocatalytic activity of chitosan-based nanocomposites added titanium oxide nanoparticles", Macromol. Res. **24**, 51–59 (2016). https://doi.org/10.1007/s13233-016-4008-6
[59] K.T. Karthikeyan, A. Nithya, and K. Jothivenkatachalam, "Photocatalytic and antimicrobial activities of chitosan-TiO_2, nanocomposite", Int. J. Biol. Macromol. **104**, 1762–1773 (2017).
[60] T. Kamal, Y. Anwar, S.B. Khan, M.T.S. Chani, and A.M. Asiri, "Dye adsorption and bactericidal properties of TiO_2/Chitosan coating layer", Carbohydr. Polym. **148**, 153–160 (2016). https://doi.org/10.1016/j.carbpol.2016.04.042
[61] H. Chang, J. Lv, H. Zhang, B. Zhang, W. Wei, and Y. Qiao, "Photoresponsive colorimetric immunoassay based on chitosan modified AgI/TiO_2 heterojunction for highly sensitive chloramphenicol detection",Biosens. Bioelectron. **87**, 579–586 (2017). https://doi.org/10.1016/j.bios.2016.09.002
[62] W. Xu, W. Xie, X. Huang, X. Chen, N. Huang, X. Wang, and J. Liu, "The graphene oxide and chitosan biopolymer loads TiO_2 for antibacterial and preservative research", Food Chem. **221**, 267–277 (2017). https://doi.org/10.1016/j.foodchem.2016.10.054
[63] A. Mohandas, S. Deepthi, R. Biswas, and R. Jayakuma, "Chitosan based metallic nanocomposite scaffolds as antimicrobial wound dressings", Bioact. Mater. **3**, 267–277 (2018). https://doi.org/10.1016/j.bioactmat.2017.11.003
[64] U. Siripatrawan, and P. Kaewklin, "Fabrication and characterization of chitosan-titanium dioxide nanocomposite film as ethylene scavenging and antimicrobial active food packaging", Food Hydrocoll. **84**, 125–134 (2018). https://doi.org/10.1016/j.foodhyd.2018.04.049
[65] A. Razzaz, S. Ghorban, L. Hosayni, M. Irani, and M. Aliabadi, "Chitosan nanofibers functionalized by TiO_2 nanoparticles for the removal of heavy metal ions", J. Taiwan Inst. Chem. Eng. **58**, 333–343 (2015). https://doi.org/10.1016/j.jtice.2015.06.003
[66] A. Spoială, C.-I. Ilie, G. Dolete, A.-M. Croitoru, V.-A. Surdu, R.-D. Truşcă, L. Motelica, O.-C. Oprea, D. Ficai, A. Ficai, E. Andronescu, and L.-M. Diţu, "Preparation and characterization of chitosan/TiO_2 composite membranes as adsorbent materials for water purification", Membranes **12**, 804 (2022). https://doi.org/10.3390/membranes12080804
[67] R. Saravanan, J. Aviles, F. Gracia, E. Mosquera, and V.K. Gupta, "Crystallinity and lowering band gap induced visible light photocatalytic activity of TiO_2/CS (Chitosan) nanocomposites", Int. J. Biol. Macromol. **109**, 1239–1245 (2018). https://doi.org/10.1016/j.ijbiomac.2017.11.125

[68] H.H. Ibrahim, A.M. Abdelghany, M.H. Gaber, and S.A. Ali, "Optical and physical characteristics of chitosan/silver vanadate nanocomposites", Opt. Quantum Electron. **56**, 435 (2024). https://doi.org/10.1007/s11082-023-05979-z
[69] E. Filippo, C. Carlucci, A.L. Capodilupo, P. Perulli, F. Conciauro, G.A. Corrente, G. Gigli, and G. Ciccarella, "Enhanced photocatalytic activity of pure anatase $TiO_2$and Pt-TiO_2nanoparticles synthesized by green microwave assisted route", Mater. Res. **18**, 473–481 (2015). http://dx.doi.org/10.1590/1516-1439.301914
[70] P. Mujeeb Rahman, V.M. Abdul Mujeeb, K.Muraleedharan, and S.K. Thomas, "Chitosan/nano ZnO composite films: enhanced mechanical, antimicrobial and dielectric properties", Arab J. Chem. **11**, 120 (2018). https://doi.org/10.1016/j.arabjc.2016.09.008
[71] N.D. Alharbi, "Synthesis of composites from hydroxypropyl cellulose:iron (III) oxide nanoparticles", Polym. Polym. Compos. **31**, 1–12 (2023). https://doi.org/10.1177/09673911221149548
[72] N.D. Alharbi, H.H. Amer, N.A. El-Zaher, and O.W. Guirguis,"Saudi cotton fabrics treated with chitosan and different concentrations of ZnO nanoparticles: Preparation, characterization, and demonstration", Fiber. Polym. **24**, 537–554 (2023). https://doi.org/10.1007/s12221-023-00035-9
[73] A. Olaru, T.Măluțan, U.C. Marta, M. Geba, and L. Stratulat, "Structural changes in hemp fibers following temperature, humidity and UV or gamma-ray radiation exposure", Cellulose Chem. Technol. **50**, 31–39 (2016).
[74] N.A. El-Zaher, G.T. El-Bassyouni, M.A.Esawy, and O.W. Guirguis, "Amendments of the structural and physical properties of cotton fabrics dyed with natural dye and treated with different mordants", J. Nat. Fibers, **18**, 1247–1260 (2021). https://doi.org/10.1080/15440478.2019.1689884
[75] I. Corazzari, R. Nisticò, F. Turci, M.G. Faga, F. Franzoso, S.Tabasso, and G. Magnacca, "Advanced physico-chemical characterization of chitosan by means of TGA coupled on-line with FTIR and GCMS: Thermal degradation and water adsorption capacity", Polym. Degrad. Stab. **112**, 1–9 (2015). https://doi.org/10.1016/j.polymdegradstab.2014.12.006
[76] I. Ozsoy, A. Demirkol, A. Mimaroglu, H. Unal, and Z. Demir, "The influence of micro-and nano-filler content on the mechanical properties of epoxy composites", Stroj. Vestn. J. Mech. E, **61**, 601 (2015). https://doi.org/10.5545/SV-JME.2015.2632
[77] L. Cui, S. Gao, X. Song, L. Huang, H. Dong, J. Liu, F. Chen, and S. Yu, "Preparation and characterization of chitosan membranes", RSC Adv. **8**, 28433–28439 (2018). https://doi.org/10.1039/c8ra05526b
[78] A. Al-Harrasi, S.Bhtaia, M.S. Al-Azri, H.A. Makeen, M. Albratty, H.A. Alhazmi, S. Mohan, A. Sharma, and T. Behl, "Development and characterization of chitosan and porphyran based composite edible films containing ginger essential oil", Polymers, **14**, 2518 (2022). https://doi.org/10.3390/polym14091782
[79] N.A. El-Zaher, M.S. Melegy, and O.W. Guirguis, "Thermal and structural analyses of PMMA/TiO_2 nanoparticles composites", Nat. Sci. **6**, 859 (2014). https://doi.org/10.4236/NS.2014.611083
[80] V.G.L. Souza, J.R.A. Pires, C. Rodrigues, P.F. Rodrigues, A. Lopes, R.J. Silva, J. Caldeira, M.P. Duarte, F.B. Fernandes, I.M.Coelhoso, and A.L. Fernando, "Physical and morphological characterization of chitosan/montmorillonite films incorporated with ginger essential oil", Coatings, **9**, 700 (2019). https://doi.org/10.3390/coatings9110700
[81] V. Alizadeh, H. Barzegar, B. Nasehi, and V. Samavati, "Development of a chitosan-montmorillonite nanocomposite film containing Satureja hortensis essential oil", Iran. Food Sci. Technol. Res. J. **13**, 131–143 (2018). https://doi.org/10.22067/ifstrj.v1396i13.64248
[82] E.M. Abdelrazek, I.S. Elashmawi, and S. Labeeb, "Chitosan filler effects on the experimental characterization, spectroscopic investigation and thermal studies of PVA/PVP blend films", Physica B, **405**, 2021–2027 (2010). https://doi.org/10.1016/j.physb.2010.01.095
[83] A.W. Coats, and J.P. Redfern, "Kinetic parameters from thermogravimetric data", Nature, **201**, 68–69 (1964).
[84] T. Fahmy, E.O. Abdelmuttlib, M.I. Abdelhamid, W.B. Elsharkawy, Z.M. Elqahtani, and M.T. Ahmed, "TSDC of irradiated and non-irradiated cellulose acetate", Egypt. J. Chem. **64**, 2453–2468 (2021). https://doi.org/10.21608/EJCHEM.2021.57068.3228
[85] W.B. Elsharkawy, M.T. Ahmed, E.O. Abdelmuttlib, Z.M. Elqahtani, M.A. Azzam, and T. Fahmy, "Effect of γ-irradiation on thermally stimulated depolarization current spectra of polyethylenegrafted-poly(acrylic acid)", Radiat. Eff. Defects Solids, **177**, 671–687 (2022). https://doi.org/10.1080/10420150.2022.2073880
[86] Y. Amaregouda, K. Kamanna, and T. Gasti, "Biodegradable polyvinyl alcohol/carboxymethyl cellulose composite incorporated with l-alanine functionalized MgO nanoplates: Physico-chemical and food packaging features", J Inorg OrganometPolym Mater. **32**, 2040–2055 (2022). https://doi.org/10.1007/s10904-022-02261-9
[87] A.M. El-naggar, Z.K. Heiba, M.B. Mohamed, A.M. Kamal, G. Lakshminarayana, and M. Ali Shar, "Structural, linear and nonlinear optical properties of poly (vinyl alcohol) (PVA)/polyethylene glycol (PEG)/SnS_2:Y nanocomposite films", Optik, **258**, 168941 (2022). https://doi.org/10.1016/j.ijleo.2022.168941
[88] N.A. Abdel-Zaher, G.T.El-Bassyouni,M.T.H.Moselhey, and O.W. Guirguis, "Structural, thermal and optical modifications of chitosan due to UV-ozone irradiation", Egypt. J. Chem. **61**, 447–460 (2018). https://doi.org/10.21608/ejchem.2018.2904.1241
[89] N.D. Alharbi, and O.W. Guirguis, "Macrostructure and optical studies ofhydroxypropylcellulose in pure and nano-composites forms", Results Phys. **15**, 102637 (2019). https://doi.org/10.1016/j.rinp.2019.102637
[90] S.B. Aziz, "Morphological and optical characteristics of chitosan$_{(1-x)}$:Cu^o_x ($4 \le x \le 12$) based polymer nano-composites: Optical dielectric loss as an alternative method for Tauc's model", Nanomaterials, **7**, 444 (2017). https://doi.org/10.3390/nano7120444
[91] A.S. Hassanien, and I. Sharma, "Synthesis, analysis, and characterization of structural and optical properties of thermally evaporated chalcogenide a-Cu-Zn-Ge-Se thin films", Mater. Chem. Phys. **311**, 128524 (2024). https://doi.org/10.1016/j.matchemphys.2023.128524
[92] D.J. Borah, and A.T.T. Mostako, Investigation on dispersion parameters of Molybdenum Oxide thin films via Wemple–DiDomenico (WDD) single oscillator model", Appl. Phys. A 126, 818–825 (2020). https://doi.org/10.1007/s00339-020-03996-3
[93] D.A. Nasrallah, T.H. AlAbdulaal, H.Y. Zahran, I.S. Yahia, and M.I. Mohammed, "Investigation of linear and nonlinear optical characterization of triple blended polymers incorporated with varying content of eriochrome black T dye for low-cost optical technologies and limiting absorption", Mater. Sci. Semicond. Process. **175**, 108179 (2024). https://doi.org/10.1016/j.mssp.2024.108179

[94] J. Tauc, *Optical Properties of Amorphous Semiconductors, Amorphous and Liquid Semiconductors*, (Plenum Press, New York, 1979).
[95] F.M. Amin, H. Abdel-Khalek, A.M. El-Sagheer, M. Abd-El Salam, and A.M. El-Mahalawy, "Detailed investigations on structural, spectroscopic, and optoelectronic properties of Ethyl Nile Blue thin films", Phys. B: Conden. Matter, **642**, 414141 (2022). https://doi.org/10.1016/j.physb.2022.414141
[96] A.M. Ismail, M.I. Mohammed, and E.G. El-Metwally, "Influence of gamma irradiation on the structural and optical characteristics of Li ion-doped PVA/PVP solid polymer electrolytes", Indian J. Phys. **93**, 175–183 (2019). https://doi.org/10.1007/s12648-018-1286-1
[97] O.Gh. Abdullah, S.B. Aziz, and M.A. Rasheed, "Structural and optical characterization of PVA:$KMnO_4$ based solid polymer electrolyte", Results Phys. **6**, 1103–1108 (2016). https://doi.org/10.1016/j.rinp.2016.11.050
[98] M.T. Ahmed, A. Sarhan, Z.M. Elqahtani, W.B. Elsharkawy, M.A. Azzam, and T. Fahmy, "Linear and non-linear optical parameters of copper chloride doped poly (vinyl alcohol) for optoelectronic applications", Egypt. J. Chem. **65**, 99–108 (2022). https://doi.org/10.21608/ejchem.2022.105927.4878
[99] M. Shkir, V. Ganesh, S. AlFaify, I.S. Yahia, and H.Y. Zahran, "Tailoring the linear and nonlinear optical properties of NiO thin films through Cr^{3+} doping", J. Mater. Sci.: Mater. Electron. **29**, 6446–6457 (2018). https://doi.org/10.1007/s10854-018-8626-y
[100] F.M. Ali, "Structural and optical characterization of [(PVA:PVP)-Cu^{2+}] composite films for promising semiconducting polymer devices", J. Mol. Struct. **1189**, 352–359 (2019). https://doi.org/10.1016/j.molstruc.2019.06.055
[101] S.H. Wemple, and M.D. DiDomenico Jr.,"Behavior of the electronic dielectric constant in covalent and ionic materials", Phys. Rev. B, **3**, 1338–1351 (1971). https://doi.org/10.1103/PHYSREVB.3.1338
[102] H.Y.S. Al-Zahrani, "Synthesis, optical and optoelectrical analysis of the Cu_2CoSnS_4 thin films as absorber layer for thin-film solar cells", J. Mater. Sci. Mater. Electron. 31, 6900–6909 (2020). https://doi.org/10.1007/s10854-020-03252-7
[103] L.M. El Radaf, and A.S. Hassanien, "Effect of thickness on structural, optical, and optoelectrical properties of sprayed $CuInSnS_4$ thin films as a new absorber layer for solar cells", Physica B, **659**, 414867 (2023). https://doi.org/10.1016/j.physb.2023.414867
[104] T.S. Soliman, S.A. Vshivkov, and S.I. Elkalashy, "Structural, linear and nonlinear optical properties of Ni nanoparticles–polyvinyl alcohol nanocomposite films for optoelectronic applications", Opt. Mater. **107**, 110037 (2020). https://doi.org/10.1016/j.optmat.2020.110037
[105] A.S. Hassanien, "Intensive linear and nonlinear optical studies of thermally evaporated amorphous thin Cu-Ge-Se-Te films", J. Non-Cryst. Solids, **586**, 121563 (2022). https://doi.org/10.1016/j.jnoncrysol.2022.121563
[106] S.H. Alotaibi, A.S. Radwan, Y.K. Abdel-Monem, and M.M. Makhlouf, "Synthesis, thermal behavior and optical characterizations of thin films of a novel thiazole azo dye and its copper complexes", Spectrochimica Acta Part A: Molecular and Biomolecular Spectroscopy, **205**, 364–375 (2018). https://doi.org/10.1016/j.saa.2018.07.043
[107] T.A. Taha, A.A. Azab, and M.A., Sebak, "Glycerol-assisted sol-gel synthesis, optical, and magnetic properties of $NiFe_2O_4$ nanoparticles", J. Mol. Struct. **1181**, 14–18 (2019). https://doi.org/10.1016/j.molstruc.2018.12.075
[108] M. Aslam, M. Ali Kalyar, and Z. Ali Raza, "Graphene oxides nanosheets mediation of poly(vinyl alcohol) films in tuning their structural and opto-mechanical attributes", J. Mater. Sci. Mater. Electron. **28**, 13401-13413 (2017). https://doi.org/10.1007/s10854-017-7177-y
[109] Z.K. Heiba, A.M. El-naggar, A.M. Kamal, O.H. Abd-Elkader, and M.B. Mohamed, "Optical and dielectric properties of PVC/TiO_2/TBAI ionic liquid polymer electrolyte", Opt. Mater. **139**, 113764 (2023). https://doi.org/10.1016/j.optmat.2023.113764

ПОКРАЩЕННЯ МОЛЕКУЛЯРНО-СТРУКТУРНИХ ТА ЛІНІЙНИХ/НЕЛІНІЙНИХ ОПТИЧНИХ ХАРАКТЕРИСТИК НАНОКОМПОЗИТНИХ ПЛІВОК ХІТОЗАНУ/ДІОКСИДУ ТИТАНУ ДЛЯ ПАКУВАННЯ ТА ОПТОЕЛЕКТРОННИХ ЗАСТОСУВАНЬ

Осіріс В. Гіргіс[a], Найлаа Д. Алхарбі[b]
[a]Відділ біофізики, Факультет природничих наук, Каїрський університет, Гіза, Єгипет
[b]Відділ фізичних наук, Науковий коледж, Університет Джидди, Джидда, Саудівська Аравія

Поточне дослідження спрямоване на синтез та характеристику нанокомпозитних плівок хітозану та діоксиду титану з точки зору молекулярної структури, теплових та оптичних властивостей для використання в упаковці продуктів та оптоелектронних застосувань. Інфрачервона спектроскопія з перетворенням Фур'є (FTIR) була використана для вивчення взаємодії між TiO_2-NPs і хітозаном, і аналіз підтвердив, що TiO_2-NPs взаємодіяли з хітозаном і продемонстрували хорошу сумісність. Диференціальна скануюча калориметрія та термогравіметричний аналіз показали, що збільшення концентрації TiO_2-NP покращує термічну стабільність нанокомпозитів. Лінійні оптичні властивості в діапазоні UV-Vis (200–800 нм) вимірювали спектрофотометрично. Нижче 400 нм спектри пропускання нанокомпозитів демонструють знижений ступінь прозорості, що вказує на їх здатність повністю блокувати пропускання УФ-світла. Модель Таука була використана для ідентифікації типів електронних переходів у зразках. Модель одного осцилятора була використана для дослідження енергії та параметрів дисперсії. Також були досліджені нелінійно-оптичні властивості. UV-Vis в області (360-410 нм), аналіз показав, що збільшення концентрації TiO_2-NPs від 0 до 12 мас. % зменшує край поглинання з 2,716 до 2,043 еВ, зменшує пряме (3,282 до 2,798 еВ) і непрямі (від 2,417 до 1,581 еВ) енергетичні заборонені зони, збільшили енергію Урбаха з 0,692 до 1,295 еВ, зменшили енергію дисперсії з 11,324 до 5,621 еВ, зменшили енергію одного осцилятора з 6,308 до 5,393 еВ і покращили інші лінійні та нелінійні параметри . Результати підтверджують використання нанокомпозитних плівок CS/TiO_2 в пакувальній промисловості та різноманітних оптичних застосуваннях.

Ключові слова: *хітозан; наночастинки TiO_2; нанокомпозити хітозан/TiO_2; FTIR аналіз; термостабільність; лінійні/нелінійні оптичні властивості*